Brain–muscle communication prevents muscle aging by maintaining daily physiology

Arun Kumar[1*‡], Mireia Vaca-Dempere[1*], Thomas Mortimer[2], Oleg Deryagin[1], Jacob G. Smith[1,3], Paul Petrus[3,4], Kevin B. Koronowski[3], Carolina M. Greco[3,5], Jessica Segalés[1], Eva Andrés[1], Vera Lukesova[1], Valentina M. Zinna[2], Patrick-Simon Welz[6], Antonio L. Serrano[1,7^], Eusebio Perdiguero[1,7^], Paolo Sassone-Corsi[3], Salvador Aznar Benitah[2,8‡], Pura Muñoz-Cánoves[1,7,8 ‡]

1. Universitat Pompeu Fabra (UPF), Department of Medicine and Life Sciences (MELIS), 08003 Barcelona, Spain.

2. Institute for Research in Biomedicine (IRB), Barcelona), The Barcelona Institute of Science and Technology, Barcelona, Spain.

3. Center for Epigenetics and Metabolism, U1233 INSERM, Department of Biological Chemistry, University of California, Irvine, CA, USA, 92697.

4. Department of Medicine (H7), Karolinska Institutet, Stockholm 141 86, Sweden.

5. Department of Biomedical Sciences, Humanitas University and Humanitas Research Hospital IRCCS, Via Manzoni 56, 20089, Rozzano (Milan), Italy.

6. Hospital del Mar Medical Research Institute (IMIM), Cancer Research Programme, 08003 Barcelona, Spain.

7. Altos Labs Inc, San Diego Institute of Science, San Diego, CA 92121, USA.

8. Catalan Institution for Research and Advanced Studies (ICREA), 08010, Barcelona, Spain.

* Equal first-author contribution

^ Equal contribution

‡ Correspondence:

arunigib@gmail.com;
salvador.aznar-benitah@irbbarcelona.org;
pmunozcanoves@altoslabs.com

Abstract

A molecular clock network is crucial for daily physiology and maintaining organismal health. We examined the interactions and significance of intra-tissue clock networks in muscle tissue maintenance. In arrhythmic mice showing premature aging, we created a basic clock module involving a central and a peripheral (muscle) clock. Reconstituting the brain–muscle clock network is sufficient to preserve fundamental daily homeostatic functions and prevent premature muscle aging. However, achieving whole muscle physiology requires contributions from other peripheral clocks. Mechanistically, the muscle peripheral clock acts as a gatekeeper, selectively suppressing detrimental signals from the central clock while integrating important muscle homeostatic functions. Our research reveals the interplay between the central and peripheral clocks in daily muscle function and underscores the impact of eating patterns on these interactions.

MAIN TEXT

Organismal health relies on the precise performance of daily tissue functions, which are governed by a molecular oscillatory system present in all cells (*1–3*). This intricate oscillatory system is thought to be hierarchically organized and coordinated, to ensure the overall coherence of the organism. At the core of this system is the central clock located in the suprachiasmatic nucleus (SCN) of the brain, which receives daily light cues and communicates with peripheral tissues, enabling the synchronization of peripheral tissue clocks for optimal function (*4*, *5*). In addition to light signals, the SCN also integrates external cues, such as activity–rest cycles, feeding–fasting rhythms, and circadian fluctuations in body temperature, and transmits this information to other tissues (*6–8*). Nevertheless, peripheral clocks can also autonomously receive and respond to specific external cues (*9–12*). The mechanisms underlying this circadian organization are not fully known but likely require active communication between all tissue clocks to execute their daily functions correctly and maintain organism physiology(*6*, *7*, *13*, *14*). Lifestyle changes, disease, and aging are known factors that can perturb circadian clock functions, with detrimental consequences. For instance, in older individuals, the SCN network is disrupted, marked by the loss of GABAergic axon terminals and receptors in neurons. This disruption results in a reduction in the amplitude of the SCN electrical activity rhythms and phase desynchronization. These changes correlate with a decline in overall activity levels, sleep/wake cycle disruptions, and a decline in physiological functions (*15–18*). Peripheral tissues such as the liver and stem cells in muscle and skin reprogram their daily functions, likely to deal with age-associated stressors (*19*, *20*).

Skeletal muscle, the most abundant tissue, is vital not only for the mobility and autonomy of individuals but also for performing essential homeostatic metabolic functions of the body. Aging is associated with a decline in the mass, strength, and function of skeletal muscle, which can lead to sarcopenia, a wasting process accompanied by low-grade inflammation, impaired proteostasis, dysfunctional mitochondria, and oxidative and metabolic stress (*21*, *22*). Circadian clock disruption is also linked to old age–associated ailments and metabolic disorders (*23*, *24*). Consistent with this, mice with a global deficiency in circadian clock genes (such as *Bmal1*) are arrhythmic and show premature aging, with altered metabolism and muscle wasting, although a developmental function of *Bmal1* has been proposed to contribute to this phenotype (*25–28*). All in all, the contributions of clock networks to maintaining daily muscle rhythmic physiology are largely unknown.

We investigated the interactions between the brain and muscle clocks and their roles in maintaining proper daily muscle physiology. We sought to determine whether the disruption of these interactions contributes to muscle aging phenotypes. To achieve this, we examined the

autonomy and interdependency of the central and peripheral muscle tissue clocks. The simultaneous activities of the central and peripheral clocks prevented premature muscle aging in clockless mice by sustaining essential physiological functions of rhythmic muscle. Signaling from the SCN clock was necessary to drive the rhythmic muscle clock. However, the muscle clock received signals from the SCN clock and effectively filtered them out, acting as a gatekeeper. This gatekeeping function of the peripheral clock over the central clock was required to prevent sarcopenia. Intriguingly, the imposition of a feeding regime associated with correct circadian rhythm (e.g., time-restricted feeding) restored muscle physiology and the daily circadian rhythm in physiologically aged mice as well as in prematurely aged, clock-deficient mice with only the muscle clock. These findings highlight the critical importance of interactions within the circadian clock circuitry in maintaining organism physiology.

RESULTS

Brain–muscle clock communication maintains adult muscle homeostasis and prevents premature muscle sarcopenia during aging

We aimed to address several unresolved questions related to regulation of circadian rhythms and their impact on bodily functions. Specifically, we sought to investigate: i) the degree of autonomy exhibited by tissue circadian outputs; ii) the importance of communication networks between central–peripheral or peripheral–peripheral clocks in organism physiology; iii) the role of circadian rhythm disruptions in aging phenotypes; and iv) whether restoring circadian disruptions could potentially decelerate or reverse muscle aging. Studies on mice with global or tissue-specific genetic deficiencies in core clock components have provided minimal information about these questions (*9, 25–29*).

We used our global *Bmal1* knockout (KO) mouse model that prevents *Bmal1* expression (*Bmal1*-stopFL mice) but allows endogenous *Bmal1* to be reconstituted in any tissue of choice through Cre-mediated recombination (*9–11*). We generated three new mouse lines by crossing *Bmal1* KO mice with mice expressing Cre recombinase under the regulation of i) the *Acta1* (Hsa) promoter, which reconstitutes endogenous *Bmal1* in skeletal muscle ("muscle-RE"); ii) the synaptotagmin10 (*Syt10*) promoter, which reconstitutes *Bmal1* predominantly in the SCN of the brain ("brain-RE") (*30*); and iii) both the *Acta1* and *Syt10* promoters, which reconstitutes *Bmal1* in both the SCN and muscle ("RE/RE") (Fig. 1A and fig. S1A). Muscle or brain-specific expression of BMAL1 was confirmed in muscle-RE (fig. S1B) and brain-RE mouse models (*30*). All mice were housed under standard 12:12 hour light/dark (L/D) cycles. Bmal1 mutants exhibit early aging signs, such as muscle mass and strength loss (sarcopenia), at around 10 weeks and start dying at around 30

weeks (*9, 25*). Thus, we studied the early and late stages of muscle decline of these mice at 10 and 26 weeks, respectively, and analyzed their muscle phenotype, locomotion, and metabolic patterns.

As compared to wild-type (WT) mice, 26-week-old KO mice showed reduced body weight (Fig. 1B) and stronger signs of muscle deterioration than 10-week-old KO mice, including a general reduction of myofiber size that affected predominantly fast-type IIB fibers (characteristic of muscle wasting and sarcopenia) and increased collagen accumulation (fibrosis) (Fig. 1, C and D, and fig. S1G). Additional signs of muscle aging included the presence of small embryonic myosin heavy chain (eMHC)-expressing fibers, central-nucleated fibers (indicators of muscle damage), infiltrating inflammatory cells, and loss of muscle force (Fig. 1, C and D, and fig. S1, C to F). Restoring *Bmal1* expression in either muscle or brain mildly attenuated some traits of muscle aging (Fig. 1, C and D, and fig. S1G). However, the dual reconstitution of muscle and brain clocks (in RE/RE mice) prevented the sarcopenia-like phenotype, as shown by the preservation of muscle mass, force, and size of the IIB myofibers, reduced amounts of fibrosis, fewer central-nucleated fibers, and diminished macrophage infiltration. We conclude that the abnormal muscle phenotypes arose from the absence of brain–muscle communication, and that maintaining key processes in adult muscle physiology strongly depended on central–peripheral (brain–muscle) clock networks.

Compared to WT mice, both KO and muscle-RE mice displayed arrhythmic daily patterns of activity/inactivity, oxygen consumption, energy expenditure, and glucose and lipid oxidation (Fig. 1E and fig. S1, H and I). In contrast, both brain-RE and RE/RE mice recovered these rhythmic parameters to a large degree, with rhythmic solid locomotor activity and oxygen consumption during the active time (ZT12 to ZT0) (Fig. 1F and fig. S1, H and I). This demonstrates that the central clock is autonomous in driving daily locomotor and metabolic behavior, and that the profound muscle alterations in brain-RE mice were not caused by defects in locomotor activity rhythms but rather by the absence of the intrinsic muscle clock. Critically, this suggests that communication between the SCN and the muscle clocks is required to maintain the tissue's homeostasis and to prevent premature muscle sarcopenia/aging.

The brain–muscle communication node sustains essential homeostatic functions but requires other peripheral clocks for full daily muscle physiology

To correlate muscle physiology and aging alterations with circadian outputs in the distinct mouse genotypes, we obtained the transcriptomes of muscle from WT, KO, muscle-RE, brain-RE, and RE/RE mice, at 10 or 26 weeks of age. Samples were collected every 4 hours for 24 hours and then analyzed by RNA-sequencing (RNA-seq) (fig. S2A). Principal component analysis (PCA) of all samples showed that muscle-RE and RE/RE transcriptomes clustered closer to those from

WT animals than to those from KO, but that the brain-RE transcriptome was more similar to that from KO animals (Fig. 2A and fig. S2B). To identify circadian muscle transcripts in each single genotype, we applied two independent, non-parametric rhythmic methods, JTK-Cycle algorithm ($P < 0.05$) (*31*) and RAIN ($P < 0.01$) (*32*), which ensures robust and reliable detection of the circadian transcriptome in each genetic mouse model (fig. S2, C to E, and tables S1 and S2). To define rhythmic transcript differences between genetic models, we applied the statistical framework dryR (differential rhythmicity analysis in R) to assess a parametric model-based differential rhythmicity of a time series with two or more conditions (table S3) (*33*).

Muscle from both 10- and 26-week-old muscle-RE mice showed expression of core-clock genes but not their rhythmic oscillations (i.e., *Bmal1, Per1-3, Cry1-2, Rorc,* and *Nr1d1*) (Fig. 2B and fig. S3A), indicating that the muscle peripheral clock was not fully autonomous. In brain-RE mice, only *Per1-2* and *Cry1-2* at 10 weeks, and *Per1-2* and *Cry1* at 26 weeks, showed rhythmic expression in muscle (Fig. 2B and fig. S3A). In the muscle of RE/RE mice, the clock core components oscillated with amplitudes, phases, and periods almost identical to those from WT mice at both ages (Fig. 2B and fig. S3A). These results also indicate that the muscle peripheral clock does not function autonomously. Instead, it relies on the brain–muscle clock network to drive the oscillation of the muscle circadian machinery. Thus, the brain–muscle communication appears to be necessary and sufficient to drive oscillation of the muscle circadian machinery.

Of the 1716 rhythmic transcripts in WT muscle, only 183 or 150 were also present in the muscle of muscle-RE mice (and not of KO mice) at 10- or 26-weeks of age, respectively, indicating that the expression of this small fraction of genes depended on the muscle clock (Fig. 2C and table S3). However, these transcripts had reduced amplitudes and altered phases as compared to those in WT mice (Fig. 2D). In contrast, a high fraction of WT rhythmic genes remained rhythmic in muscle of brain-RE mice ($n = 695$ and $n = 418$ at 10 and 26 weeks of age, respectively) (Fig. 2E); however, these genes also showed altered phases and slightly increased amplitudes (Fig. 2F). Muscle-autonomous rhythmic genes (e.g., genes that did not require the central brain clock) ($n = 183$) were enriched in stress and inflammatory pathways (such as sumoylation of DNA repair proteins, mitogen-activated protein kinase [MAPK] and interleukin signaling), basic cell transcription, and circadian regulation (Fig. 2I). Finally, brain-autonomous rhythmic genes ($n = 695$) were enriched in a broader array of signal transduction pathways associated with stress responses and circadian processes (Fig. 2J).

Muscle of RE/RE mice retained 310 and 175 of the WT circadian genes at 10 and 26 weeks of age, respectively, and these transcripts exhibited normal phase and amplitude distribution (Fig. 2, G and H, and table S3). Genes that only required the brain–muscle communication for daily rhythmicity ($n = 310$) included those with enriched functions in the regulation of muscle growth and proteostasis, such as the forkhead box O (FoxO)-mediated transcription regulation (*Akt2,*

FoxO4, and *Foxk1*) and tumor necrosis factor-alpha (TNFα) and nuclear factor kappa B (NF-κB) signaling (negative regulation of myofiber growth), AMP-activated protein kinase (AMPK), phosphoinositide 3-kinase-AKT-mammalian target of rapamycin (PI3K-AKT-mTOR) signaling (*Prkca* and *Pld1)* (positive regulation of myofiber growth), autophagy (regulation of myofiber proteostasis) (*34*), myogenesis (e.g., *Myog, Myod1* [the master regulator of myogenic differentiation], and *Tcap*) (*35*), and metabolic functions, such as insulin/glucose and phospholipid metabolism (*Pik3ca, Fbxo30,* and *Pnpla7*) (Fig. 2K and fig. S3B) (*34*). Transcription factor analyses demonstrated an enrichment in motifs conferring regulation by E2F, EGR, IRF, or MECP2, as well as the presence of the BMAL1 motif, suggesting the involvement of these factors in circadian transcription regulation (fig. S3C and table S4). This partial circadian recovery in muscle of RE/RE mice may account for the maintenance of muscle homeostasis and the prevention of premature aging (Fig. 1, C and D), reinforcing the notion that *Bmal1* in muscle must be expressed rhythmically (driven by the SCN input) to rescue the muscle aging defect of the KO mice.

However, >50% of genes were rhythmic only in muscle of WT mice at 10- or 26-weeks of age. In other words, the presence of the isolated brain–muscle communication module (with no other peripheral clocks) did not suffice to restore the circadian expression of these genes (fig. S3, D and E), which were enriched in functions such as cell–cell contact, protein phosphorylation, signal transduction cascades (i.e., focal adhesion or EGF and second-messengers signaling), and pathways involved in muscle homeostasis (e.g., thyroid hormone, responses to oxygen levels [hypoxia], and immune system regulation) (*36–38*) (fig. S3F). These findings indicate that i) the brain–muscle clock network generates adequate signals to drive a rhythmic muscle clock and to bolster its rhythmic gene amplitude and output, and ii) this clock communication regulates essential muscle physiology functions with the correct daily timing and prevents premature sarcopenia. Nonetheless, our results underscore that muscle communication with other peripheral clocks is needed for the complete circadian gene program that supports key physiological functions in muscle.

The muscle peripheral clock acts as a gatekeeper for signals from the central clock that regulate mitochondrial metabolism and homeostasis

The unexpectedly high number of distinct muscle rhythmic transcripts (n = 1373) detected only when the brain clock was present (brain-RE mice) (Fig. 3, A and B) indicated that there are brain-driven, *Bmal1*-independent oscillations in muscle (*39, 40*). However, these brain-driven transcripts had altered amplitudes and misaligned oscillation phases: most of them peaked at *zeitgeber* time (ZT) 16 to ZT18 or during the rest phase (ZT2 to ZT6), in contrast to their uniform distribution in WT mice (Fig. 3, C and D). We performed phase set enrichment analysis (PSEA)

on rhythmic genes from all genotypes to investigate the periodic phases of specific muscle processes (*41*). In WT muscle, we observed a peak expression phase during the rest time (ZT0 to ZT12) for transcripts involved in essential molecular processes, including biomolecule transport, mitochondrial functions, DNA repair, protein degradation, translation, nucleotide and lipid metabolism, mRNA splicing, and stress-related signal transduction pathways (Fig. 3E). Muscle tissue from brain-RE mice exhibited phase misalignment for the majority of these processes, with peak phases occurring during active periods. However, the additional presence of the muscle clock in RE/RE mice restored the proper alignment of muscle transcripts to that observed in WT mice (Fig. 3, E to G). Similarly, we observed a misalignment of functional processes in muscle from muscle-specific *Bmal1* KO (Mu-KO) mice, in which both central and all peripheral clocks, except muscle, are present (i.e., *Bmal1* is deleted only in muscle in an otherwise WT background); this highlights the role of the muscle clock in gating circadian processes, i.e., filtering and aligning the timing of muscle-specific functional processes (fig. S4A). Motif analysis of the de novo brain-RE transcripts (n = 1373) showed enrichment of specific ETS family transcription factors compared to that in RE/RE animals (fig. S4B). Rhythmic muscle BMAL1 can suppress ETS transcriptional activity by forming a CLOCK:BMAL1:CRY1 complex, allowing the muscle clock to regulate de novo transcripts (*39, 42*).

To evaluate muscle lipid metabolism misalignment, we measured lipid droplet density in muscle during rest and active times (day and night, respectively). Lipid droplets are a major contributor to muscle fatty acid metabolism and provide an important source of muscle energy metabolism during when animals are active (*43–46*). We observed a day/night rhythmic distribution of lipid droplets in WT muscle (with the highest at rest, and lowest during the active time) that depended on the muscle clock rhythmicity (Fig. 3H). Muscle of brain-RE mice showed phase misalignment for lipid metabolism, with a higher accumulation of lipid droplets during the active time, whereas muscle of RE/RE mice showed a distribution similar to that from WT muscle.

Muscle strongly relies on mitochondrial activity for its correct physiological functions (*47, 48*). Consistent with the observed muscle clock gatekeeping function on brain-regulated mitochondrial genes, a MitoCarta (*49*) analysis further identified mitochondria-related genes that were rhythmically expressed only in brain-RE mice (n = 179), WT mice (n = 68), or RE/RE mice (n = 12). Enrichment analysis showed that brain-RE–only (n = 1373) genes were related to fatty acid oxidation, mitochondrial TCA cycle, biogenesis, and respiration, among others (Fig. 3I), suggesting that the muscle clock can normalize and maintain timely mitochondrial functions. Efficient regulation of mitochondrial dynamics involves increasing the rate of mitochondrial fission by recruiting the fission regulator dynamin-related protein 1 (DRP1) through AMPK signaling (*50–52*). This process is essential for segregating damaged or dysfunctional mitochondria through mitophagy. In agreement with this, muscle from RE/RE animals exhibited

activated DRP1 (i.e., with S616 phosphorylation), activated AMPK (with T172 phosphorylation), and mitophagy removal of dysfunctional mitochondria, similar to muscle from WT animals. Conversely, a misalignment in the timing of mitochondrial processes was observed in brain-RE muscle, with a peak level occurring during the active time ZT16 (fig. S5, A to C).

To assess mitochondrial health in vivo in muscle of the distinct mouse lines, we transfected mouse muscle with a *MitoTimer* reporter (*53*), which emits green fluorescence for newly synthesized mitochondria and shifts to red as mitochondria accumulate oxidative stress. Compared to WT mice, KO mice and brain-RE mice exhibited an accumulation of red fluorescence, indicating mitochondrial damage (fig. S5D). Muscle-RE mice displayed more green fluorescence than KO mice, indicating that the muscle clock played a role in preserving mitochondrial integrity. The green fluorescence intensities of RE/RE and WT myofibers were similar, highlighting that brain–muscle communication was sufficient to maintain muscle mitochondrial physiology. Further, the good health status of mitochondria in aged (26-week-old) RE/RE mice correlated with the fact that these mice maintained muscle metabolism and homeostatic functions. Conversely, dysfunctional mitochondria may have contributed to the premature muscle aging observed in 26-week-old muscle-RE and brain-RE mice. This aligns with the emerging concept that dysfunctional mitochondria trigger sarcopenia during aging (*54, 55*). In sum, the muscle's gatekeeper function is vital for maintaining proper daily metabolic and homeostatic functions and for preventing sarcopenia. These findings highlight two key points: first, the central clock drives the oscillation of the muscle peripheral clock, and second, the muscle peripheral clock gates signals—that is, it filters all signals and aligns the timing of muscle-specific circadian processes, which allows it to control the expression of various circadian genes that are influenced by the brain. This gatekeeping mechanism ensures that genes are expressed appropriately during the day to support the specific metabolic requirements and physiology of muscle tissue.

Feeding–fasting cycles can substitute for the central clock to drive daily homeostatic muscle functions

The central clock can synchronize peripheral clocks through feeding signals, thereby regulating the metabolic rhythms and circadian outputs of various tissues (*56–60*). We showed that the peripheral muscle core clock does not oscillate autonomously but can be restored by reintroducing the central clock, which helps to maintain muscle physiology in clock mutants (Fig. 1, B to D). Because behavioral rhythms (such as feeding schedules) controlled by the brain clock can influence the synchronization of peripheral clocks, we investigated whether imposing a feeding–fasting regime would activate the muscle clock in the absence of the SCN and subsequently affect muscle physiology. The lack of rhythmicity in the muscle clock in muscle-RE mice allowed us to directly examine the impact of environmental signals on the muscle clock without all peripheral

clock signals. To analyze the effect of forced feeding–fasting cycles with or without clock-related input, we fed WT, KO, and muscle-RE mice under two different conditions: i) *ad libitum* feeding (ALF), with free access to food; or ii) time-restricted feeding (TRF), during which food was provided only during the active phase, for a duration of 9 to 10 hours (e.g., ZT13/14 to ZT22/23; see Methods), starting with 10-week-old mice, for about 16 weeks (fig. S6A).

Strikingly, while muscle-RE/ALF mice had arrhythmic transcriptomes, muscle-RE/TRF mice showed rhythmic oscillations for most core clock genes (i.e., *Bmal1*, *Per3*, and *Nr1d1*) and *Dbp* (fig. S6B), with similar amplitudes to those in WT/ALF mice but slightly altered phases (fig. S6, C to E). Consistent with this, PCA showed that muscle-RE/TRF transcripts clustered with WT/TRF transcripts (fig. S6F), indicating that the imposed feeding–fasting cycles can activate the muscle clock and produce adequate timing. At the muscle tissue level, certain traits were improved by TRF in muscle-RE mice but not in KO mice, such as reduced fibrosis (fig. S7A) and improved mitochondrial function. The *MitoTimer* reporter revealed that TRF enhanced mitochondrial wellness in muscle-RE/TRF myofibers to levels similar to those in WT mice (fig. S7, B and C). These findings emphasize the significance of the muscle clock for mitochondrial health and demonstrate that behavioral rhythms, such as an imposed feeding–fasting rhythm, can drive muscle functions similar to those regulated by the central clock. However, the phenotypic recovery in muscle-RE/TRF mice was only partial, as muscle fiber size and force were not fully restored (fig. S7, H and I). Thus, other peripheral tissues and the central clock may also be necessary to achieving complete muscle homeostasis. These results highlight the importance of the muscle–brain clock interaction network. Analysis of the genes in muscle-RE mice that lost their circadian expression (fig. S6G) showed that muscle-RE/TRF mice had regained the circadian expression of three groups of genes: i) 236 genes with similar amplitude as expressed in WT or RE/RE mice, indicating a dependence on both the brain and muscle clocks; ii) 261 genes with similar amplitude as expressed in WT or brain-RE mice, indicating a dependence on the brain clock; and iii) 107 genes with similar amplitude as expressed in WT mice, showing a dependency on other peripheral tissues clocks (fig. S6, H to J). Furthermore, genes in muscle-RE mice that required the brain–muscle clock communication and were driven by TRF were enriched in various pathways related to insulin signaling (e.g., *Igf2bp2* and *Insig1*), lipid metabolism (*Sphk2* and *Acer2*), circadian regulation (*Ccrn4l* and *Nrip1*), glucose metabolism (*Fbp1* and *Pfkfb4*), cell signaling (*Prkcq, Pik3ca,* and *Prkca*), and muscle growth/atrophy regulation (TNFα/NF-κB, PI3K/AKT and mTOR, and the p38 MAPK pathways). Additionally, key regulators of myogenesis (*Myod1*) (*61*) and downstream-regulated genes (*Tcap*) were also affected (fig. S6, K and L, and table S3). Finally, the genes identified as driven by the muscle clock and TRF (n = 107), independent of the brain clock, were associated with signal transduction pathways such as Hippo, EGFR signaling, and glucocorticoid receptor pathways (fig. S6M). Overall, these

findings demonstrate that TRF can partially substitute for signals derived from the central clock, driving the autonomous muscle clock and yielding shared benefits for muscle physiology.

We observed rhythmic changes in the secretion of corticosterone (the primary murine glucocorticoid) in mice with a functional SCN clock (i.e, WT, brain-RE, and RE/RE) and partially through forced feeding–fasting cycles (i.e., KO/TRF and muscle-RE/TRF) (fig. S8, A and B). This shows that the actions of the SCN clock and the adrenal gland clock were coordinated through the hypothalamic-pituitary-adrenal (HPA) axis (*62, 63*). To investigate the communication between the central and muscle peripheral clocks, we removed the adrenals glands (bilateral adrenalectomy, ADX) from RE/RE and WT mice. ADX eliminated rhythmic corticosterone production without affecting food intake (fig. S8, C and D). ADX affected the oscillation of the muscle clock genes, reducing *Bmal1* and *Per1* oscillations (*64, 65*) (fig. S8, E and F). The adrenal gland secretes catecholamines, glucocorticoids, and mineralocorticoids (*62*). To restore the disrupted gene expression in ADX mice (*66*), synthetic glucocorticoid (dexamethasone, Dex) or adrenaline (Adr) was administered intraperitoneally to WT-ADX mice daily at the beginning of the dark phase. These treatments rescued the disrupted oscillation of *Bmal1* and *Per1* (fig. S9A) (*67*) and restored the day/night oscillation of genes involved in lipid metabolism (*Acat2, Pnpla3,* and *Pdpk1*) and cell signaling (fig. S9B), although we cannot discard that a constant, non-rhythmic reinstatement of corticosterone might exert similar effects. ADX dysregulated rhythmic genes that are related to cell signaling, lipid metabolism, insulin signaling, and cytoskeleton organization in muscle (fig. S9C), and it induced fibrosis, infiltration of inflammatory cells, and muscle damage (fig. S9D), similar to the effects of disrupting the muscle clock communication. These findings highlight the role of the HPA axis in regulating the brain–muscle clock network for maintaining muscle homeostasis.

Feeding–fasting rhythms preserve daily functions and prevent sarcopenia in physiologically aged mice

The brain regulates feeding–fasting cycles by synchronizing peripheral clocks (*4, 6*). However, with aging, the brain clock deteriorates (*16–18, 68, 69*), leading to circadian misalignment and a loss of hormone receptors in the muscle (fig. S10A). We thus subjected old adult mice (66- to 74-week-old) to time-restricted feeding (TRF) (or maintained them on ad libitum feeding [ALF]) for approximately 26 weeks (fig. S10B), to determine whether this TRF regime would prevent muscle deterioration. The control group consisted of young-adult mice under ALF (hereafter, young/ALF). The core clock machinery in muscle remained rhythmic regardless of age or feeding conditions (fig. S10, C and D). Remarkably, old mice under TRF (hereafter, old/TRF) regained rhythmic gene expression (n = 452) in muscle (fig. S11, A and B), with no loss of amplitude of rhythmic genes (fig. S11, C and D), and associated functions related with muscle signaling (e.g.,

Wnt and MAPK), cytoskeleton organization, immune response, proteostasis, and metabolism (fig. S11E), resembling a youthful-like gene program. PSEA analyses revealed that rhythmic functions in old/ALF muscle exhibited a biphasic pattern with peak distribution (ZT0–ZT4 and ZT12–ZT16). In contrast, rhythmic functions in old/TRF muscle had a uniform, broader distribution that was closer to uniformly distributed processes observed in young ALF mice (fig. S11F). Thus, imposed feeding–fasting cycles prevented the age-related circadian gene misalignment normally seen in old mice and induced a youthful circadian gene program. As expected, muscle from old/ALF mice exhibited a de novo rhythmic transcriptome (n = 209), indicating that these mice had age-induced circadian reprogramming (fig. S12A). Indeed, their transcriptome was enriched for genes related to stress-related processes, such as inflammation, oxidative stress, DNA repair, protein catabolism, altered metabolism, and extracellular matrix organization (fig. S12B). These rhythmic functions showed a misaligned peak phase distribution with a major peak at ZT22 to ZT2 (fig. S12C). In stark contrast, muscle of old/TRF mice did not show atrophy (Fig. 4, A and B), increased fat accumulation (Fig. 4C), or increased fibrosis (Fig. 4D), as compared to muscle from old/ALF mice (Fig. 4, A to H). Furthermore, TRF prevented the loss of mitochondrial bioenergetics and metabolism in old muscle in vivo, as shown by the effect on succinate dehydrogenase (SDH) activity and MitoTimer output (Fig. 4E, and F). Loss of muscle strength with aging was prevented in old/TRF mice (Fig. 4I). The total rhythmic locomotor movement and diurnal rhythmic pattern of RER and VO_2 (oxygen consumption) were also maintained in old/TRF mice (fig. S12D). Overall, we conclude that deterioration of muscle functions during aging is likely caused by deterioration of the brain (SCN) central clock and can be rescued by imposed feeding–fasting (behavioral) regimes.

We investigated whether the essential minimal circadian function for muscle homeostasis depends on the brain–muscle clock network or feeding–fasting cycles. To address this, we compared the circadian transcriptomes of muscle tissue from RE/RE/ALF, muscle-RE/TRF, and old/TRF mice, all of which exhibited healthy muscle phenotypes. We identified a shared signature of 765 circadian genes among these genotypes (fig. S13A). These circadian genes exhibited similar peak phases of expression and amplitudes, indicating functional alignment (fig. S13, B and C), and were enriched for critical circadian functions whose disruption is associated with muscle aging, such as loss of muscle mass and strength. The youthful circadian functional signature included well-known regulators of energy and metabolism in muscle, including sterol regulatory element-binding protein (SREBP), insulin-like growth factor (IGF1), AKT, FoxO, AMPK, mTOR, and glycogen synthase kinase 3β (GSK3β) signaling (*24*, *70*, *71*). Furthermore, the muscle clock directly controlled functions essential for muscle mass, including genes involved in myogenic cell proliferation and differentiation, proteostasis pathways (autophagy), unfolded protein response, and immune response (fig. S13D) (*34*, *72*).

These findings highlight the importance of coordinated tissue clocks, involving both peripheral–peripheral and peripheral–central networks, in mediating the beneficial effects of feeding–fasting rhythms. We observed a complete recovery for old/TRF mice (which have all clocks), but only a partial recovery for muscle-RE/TRF mice (which only have the muscle clock). These results emphasize the critical role of the muscle clock in sarcopenia/aging and highlight the significance of synchronized tissue clocks in achieving overall tissue homeostasis.

In sum, we conclude that the muscle clock: i) plays a crucial role by setting the correct rhythms for regulating tissue-specific functions necessary to maintain muscle homeostasis and metabolism; ii) acts as a gatekeeper of the central clock signals, by limiting the expression and activity of non-essential circadian genes that could potentially harm muscle tissue; and iii) ensures that its tissue-specific functions are synchronized with the appropriate phase in a day/night-dependent manner (Fig. 4J).

DISCUSSION

The communication and coordination between tissue clocks are crucial for maintaining overall organism health (*73*, *74*). However, the mechanisms underlying this communication, and the importance of intra-tissue clock networks in muscle tissue maintenance, are still poorly understood. Our findings reveal that the central clock drives the oscillations of the peripheral muscle clock. The peripheral muscle clock, in turn, integrates these signals by sensing, interpreting, and responding to cues primarily from the central clock, and potentially from other peripheral clocks, to ensure tissue coherence. This unexpected gatekeeping function of the peripheral clock over the central clock supports the "federated model" of clock organization, which suggests that there is a decentralized network of clocks rather than a hierarchical, brain-centric network with the central clock solely controlling peripheral tissue clocks (*59*, *75*). The gatekeeper functions of the peripheral clocks are likely crucial for tissue health and overall organism function (*76*, *77*). We observed that, in the absence of an operative muscle clock, the functions driven by the central clock became erratic, while the presence of operative muscle clock filtered and corrected these erratic signals, aligning them with the correct circadian time. Additionally, the muscle clock suppressed the oscillation of over 1000 transcripts driven by the brain clock in muscle tissue and corrected the phase of critical homeostatic processes, such as mitochondrial function and lipid metabolism, as compared to those induced by the brain clock alone.

By focusing on the clock network in the brain and muscle of mice with no other clocks elsewhere, we found that this minimal clock module regulated not only daily muscle homeostatic functions but also prevented premature muscle sarcopenia and aging. Previous studies using *Bmal1*-

deficient mice have provided limited understanding, but our findings clarify the role of "rhythmic" *Bmal1* in preventing muscle aging. This is evident from the rescue of muscle aging phenotypes in mice with rhythmic *Bmal1* expression (RE/RE mice) as compared to mice with non-rhythmic *Bmal1* expression (muscle-RE mice). Specifically, rhythmic *Bmal1* driven by the brain–muscle clock network orchestrates various functions related to muscle growth, proteostasis, myogenesis, muscle architecture, and responses to metabolic cues (such as insulin, glucose, and lipids). It is interesting to note that TRF, which involves eating during the active dark phase (night feeding), could partially replace the central clock and enhanced the autonomy of the muscle clock. This finding is consistent with the observation that glucose homeostasis is restored by TRF when the muscle and liver clocks are re-established (11).

Although we cannot prove that failure in the clock network organization drives tissue decline during aging, it is well-established that the activity and output of the brain clock deteriorate with age (*16–18*, *68*, *69*, *78–80*). Aging is characterized by a shift in peak expression and decreased amplitudes of circadian genes, which contributes to the aberrant and unscheduled daily functions observed in aged tissues. These transcriptional changes have been observed in skeletal muscle and other aged tissues and cells. Our findings demonstrate that the compromised brain clock in old mice, leading to circadian misalignment, can be partially compensated by signals derived from TRF. Restoring circadian rhythm through TRF mitigated muscle loss, impaired metabolic and motor functions, and decreased muscle force in old mice.

These results highlight the potential for genetic and physiological reprogramming of the intrinsic aging clock machinery toward a more youthful state (*81–84*) and have implications for strategies to prevent circadian rhythm disruptions caused by modern lifestyles and for developing treatments for age-related diseases and aging itself.

Figure Legends

Fig. 1. Brain and muscle clocks are necessary and sufficient for circadian behavior and functional skeletal muscle. (**A**) Tissue-specific reconstitution of *Bmal1* in the different mouse models. (**B**) Body weight of the different mouse lines at 26 weeks of age**. (C)** Representative images of hematoxylin and eosin (H&E), type IIB fibers immunostaining, interstitial collagen by Sirius red, and infiltrating inflammatory CD11b+ cells immunostaining in cryosections of tibialis anterior (TA) muscle of the different mouse models at 26 weeks of age. (**D**) Quantification of cross-sectional areas (CSA) of fast type IIb fibers, collagen content by Sirius red staining, number of fibers expressing embryonic myosin, and centrally nucleated fibers in tibialis anterior (TA) muscle of the different mouse models at 26 weeks of age. Maximal specific isometric tetanic force and force-frequency curves of extensor digitorum longus (EDL) muscle of the different mouse

models are shown. (**E, F**) Activity patterns, oxygen consumption (VO_2), and metabolic parameters of the indicated mouse lines at 26 weeks of age. Scale bars: 50 μm. Results are displayed as mean ± s.e.m.; *P* values are from *t*-test (two-tailed except those for metabolic parameters, which were one-tailed). Force-frequency curves, two-way ANOVA; **P* < 0.05, ***P* < 0.01, ****P* < 0.001.

Fig. 2. Brain–muscle clock interactions drive core clock machinery, rhythmic functions, and correct phase. (**A)** Principal component analysis (PCA) of the full transcriptome of tibialis anterior (TA) muscle from WT, RE/RE, muscle-RE, brain-RE, or KO young (10- to 12-week-old) mice. (**B)** Abundance profiles of core clock genes in WT, RE/RE, muscle-RE, brain-RE, and KO young mice under LD entrainment; *n* = 3 or 4 mice at each time point. Data are presented as mean ± SD. (**C)** Phase-sorted expression heatmap showing 183 autonomous genes using dryR (BICW ≥ 0.4, amp ≥ 0.25) that oscillated only in WT and muscle-RE, but not in KO, young mice. (**D)** (top) Circular histogram plots of the peak phase (JTK_CYCLE) and (bottom) density plot showing amplitude comparison (JTK_CYCLE) of genes in D; Welch's *t*-test, *WT versus muscle-RE, *t* = 4.63, *P* = 0.0000054. (**E)** Phase-sorted expression heatmap of dryR defined (BICW ≥ 0.4, amp ≥ 0.25) 695 autonomous genes that oscillated only in WT and brain-RE (BRE), but not in KO, young mice. (**F)** (top) Circular histogram plots of the peak phase (JTK_CYCLE), and (bottom) density plot showing amplitude comparison of genes (JTK_CYCLE) in F; *WT versus brain-RE, *t* = –3.02, *P* = 0.0026. (**G)** Phase-sorted expression heatmap of dryR defined (BICW ≥ 0.4, amp ≥ 0.25) 310 RE/RE-driven genes that oscillated only in WT and RE/RE, but not in muscle-RE or brain-RE, young mice. (**H)** (top) Circular histogram plots of the peak phase, (JTK_CYCLE) and (bottom) density plot showing amplitude comparison (JTK_CYCLE) of genes in H; Welch's *t*-test, WT versus RE/RE not-significant. (**I)** Functional enrichment bubble plot showing selected gene sets; MSigDB canonical pathways enrichment (*P* < 0.05) analysis of 183 genes. (**J)** Functional enrichment bubble plot showing selected gene sets; MSigDB canonical pathways enrichment (*P* < 0.05) analysis of 695 genes. (**K)** Functional enrichment bubble plot showing selected gene sets; MSigDB canonical pathways enrichment (*P* < 0.05) analysis of 310 genes.

Fig. 3. Gating of muscle tissue rhythmic functions and phase by the peripheral muscle clock. (**A)** Number of genes classified in differential rhythmicity analysis (dryR) from WT, brain-RE, or RE/RE muscle. Blue indicates rhythmic detection; white indicates no rhythms detected between samples. 1373 unique rhythmic genes defined by dryR were detected in BRE but not in WT or RE/RE, and 597 genes were commonly rhythmic genes in all conditions (dryR; BICW ≥ 0.4, amp ≥ 0.25). (**B)** Phase-sorted expression heatmap of 1373 genes oscillating in brain-RE but not in WT or RE/RE young mice (dryR; BICW ≥ 0.4, amp ≥ 0.25). (**C)** Circular histogram plots of the peak phase (JTK_CYCLE) of the 1373 genes oscillating in brain-RE only.

(**D)** Density plot showing the 1373 rhythmic transcripts amplitude comparison (JTK_CYCLE); Welch's *t*-test, WT versus brain-RE, $t = -30.82$, $P = 5.7E-176$; WT versus RE/RE, not significant. (**E–G)** Phase set enrichment analysis (PSEA), Kuiper Q-value (vs. uniform) < 0.05 showing circular 24-hour phase distribution of aggregated muscle tissue-oriented functional categories in WT, brain-RE, and RE/RE total rhythmic genes. (**H)** Representative confocal image of individual muscle fiber shown for lipid droplets staining with BODIPY dye, laminin, and DAPI. Quantification of lipid droplet density in myofibers of tibialis anterior (TA) muscle shows rhythmic distribution in WT and RE/RE mice, and arrhythmic distribution in brain-RE, muscle-RE and KO. The box plot shows lipid droplet density distribution at ZT8 and ZT20. Boxes include 50% of data points, the line represents the median, and the whiskers extend to the maximum and minimum values; ****$P < 0.0001$; ns, not significant. (**I)** Enrichment bubble plot showing selected GSEA; MSigDB canonical pathways enrichment ($P < 0.05$) analysis of 179 mitochondrial genes (MitoCarta 3.0) that oscillate uniquely in brain-RE young mice, but not in WT or RE/RE young mice.

Fig. 4. Feeding–fasting rhythms prevent physiological age-associated rhythmic reprogramming and restore muscle dysfunctions. (**A**) Representative images for muscle functional analysis. (**B–D**) Functional analysis of tibialis anterior (TA) muscle of the indicated experimental groups. Quantification of cross-sectional area (CSA) of fast IIB fibers, (**C**) lipid content by oil Red O staining, and (**D**) collagen deposition of the indicated experimental groups. Scale bars: 50 μm except for Mitotimer, 10 μm. Results are displayed as mean ± s.e.m.; *$P \leq 0.05$, **$P < 0.01$, ***$P < 0.001$ (two-tailed *t*-test; force-frequency curves, two-way ANOVA). (**E, F**) Quantification of mitochondrial fitness by the MitoTimer reporter (with the red:green ratio showing damaged:healthy mitochondria) and myofibers with high mitochondrial enzymatic activity by succinate dehydrogenase (SDH) staining. Results are displayed as mean ± s.e.m.; *$P < 0.05$, **$P < 0.01$, ***$P < 0.001$ (two-tailed t-test). (**G**) Relative frequency of the different fast fiber subtypes (of the slow MHC IIA/X isoform and the fast MHC IIB isoform (**H**) and the distribution of fiber size (μm^2). (**I**) Force-frequency measurement curves of EDL muscle of the different mouse models. (**J**) Schematic representation of the muscle clock–gated rhythmic output that prevents sarcopenia and muscle dysfunctions. Muscle receives a plethora of signals from SCN clock or peripheral tissues but filters the unnecessary signal information to prevent non-specific rhythmic functions. The muscle clock aligns tissue-specific rhythmic functional output, which is necessary for muscle tissue homeostasis.

Figure S1. SCN and muscle clocks are necessary and sufficient to restore circadian behavior and a functional skeletal muscle. (A) Tissue-specific reconstitution of *Bmal1* in the different mouse models (**B**) Reconstitution of BMAL1 expression in skeletal muscle of muscle-RE mice.

(**C**) Increased sarcopenia features in tibialis anterior (TA) muscle of old *Bmal1* KO mice, showing the presence of centrally nucleated fibers. (**D**) Increased collagen deposition (fibrosis) in 26-week-old *Bmal1* KO mice by Sirius red staining. (**E**) Increased embryonic myosin positive ($eMHC^+$) fibers. (**F**) Increased inflammatory phenotypes as the presence of high infiltrating myeloid $CD11b^+$ cells. (**G**) Muscle morphological parameters (fast IIB fiber size, collagen deposition of the different mouse lines from young (10-week-old) mice. Scale bars: 50 μm. **H, I**) Activity patterns and metabolic parameters of 10-week-old mice over the day/night cycle. Results are mean ± s.e.m.; **P* < 0.05, ***P* < 0.01, ****P* < 0.001 (two-tailed *t*-test; metabolic parameters, one-tailed *t*-test; survival curve, Mantel-Cox test, as compared to KO).

Figure S2. Defining rhythmic gene distribution, phase, and amplitude in clock-reconstitution models. (A) Experimental setup for rhythmic collection of mice samples to obtain circadian transcriptome; tibialis anterior (TA) muscle was collected every 4 hours over 24 hours and then analyzed by RNA-sequencing (RNA-seq). *n* = 4 mice (2 male, 2 females) for each genotype (WT, KO, muscle-RE, brain-RE, and RE/RE), from 10- to 12-week-old or 26-week-old mice. (**B**) Principal component analysis (PCA) of the full transcriptome of tibialis anterior (TA) muscle of WT, RE/RE, muscle-RE, brain-RE, or KO mice at 26 weeks of age. (**C**) Upset plot showing total rhythmic genes detected in each genetic models and their comparison by two independent rhythmic analysis methods (JTK_CYCLE, RAIN). (**D**) Number of rhythmic genes in WT, RE/RE, muscle-RE, brain-RE, and KO young mice; JTK_CYCLE, $P < 0.05$, RAIN , $P < 0.01$. (**E**) Comparison of rhythmic transcriptome (WT, 10-week-old) by two independent algorithms (JTK_CYCLE, RAIN); 90% (1513) JTK rhythmic transcript similarly detected by independent RAIN analysis method.

Figure S3. Defining rhythmic gene distribution in clock-reconstitution models. (**A**) Abundance profiles of core clock genes in WT, RE/RE, muscle-RE, and brain-RE mice at 26 weeks of age. (**B**) Abundance profiles of indicated rhythmic genes in WT, RE/RE, muscle-RE, and brain-RE mice. (**C**) Enrichment of transcription factor motif using g:Profiler, (Benjamini-Hochberg FDR < 0.05, $P < 0.05$), in dryR defined (BICW ≥ 0.4, amp ≥ 0.25) 310 RE/RE-driven genes oscillating only in young WT or RE/RE, but not muscle-RE or brain-RE, mice. (**D**) Number of differential rhythmic genes classified by dryR methods in 10- to 12-week-old mice. Blue indicates rhythmic detection; white indicates no rhythms detected between samples. For WT-specific total rhythmic genes (1716), dryR comparisons of only WT and KO mice were used (dryR; BICW ≥ 0.4, amp ≥ 0.25). (**E**) Pie chart showing the proportion of total rhythmic genes identified by dryR differential rhythmic analysis of WT, RE/RE, brain-RE, muscle-RE and KO mice at 10- to 12-weeks of age. (**F**) Functional enrichment bubble plot showing selected gene sets; MSigDB canonical pathways enrichment ($P < 0.05$) analysis of WT-only rhythmic genes.

Figure S4. Gating muscle tissue rhythmic functions by the peripheral muscle clock. (A) Phase set enrichment analysis (PSEA), Kuiper Q-value (vs. uniform) < 0.05 showing circular 24-h phase distribution of aggregated muscle tissue-oriented functional categories in total rhythmic genes in muscle-specific clock-KO (Mu-KO). (**B**) Enrichment of transcription factor motif using g:Profiler (Benjamini-Hochberg FDR < 0.05, P-value <0.05), in dryR defined (BICW ≥ 0.4, amp ≥ 0.25), with 1373 genes oscillating in brain-RE but not in WT or RE/RE young mice.

Figure S5. Gating muscle tissue rhythmic functions by the peripheral muscle clock. (**A**) Quantification of active DRP1 protein (p-DRP1, phosphorylated DRP1 at Ser 616; normalized count:mean fluorescence intensity) immunostaining in cryosections of tibialis anterior (TA) muscle of the different mouse models at 10- to 12-weeks of age. (**B**) Mitophagy levels. Quantification of percentage of colocalization of mitochondria labelled with in vivo expression of the mitochondrial rxRFP and LAMP1 (lysosomal-associated membrane protein 1) in cryosections of TA muscle of the different mouse models. (**C**) Quantification of active AMPK protein (p-AMPK, AMPKα protein phosphorylation at threonine-172 [pT172], normalized count:mean fluorescence intensity) immunostaining in cryosections of TA muscle of the different mouse models at 10- to 12-weeks of age. (**D**) *In vivo* expression of the mitochondrial stress reporter MitoTimer in myofibers of TA muscle from young mice of the indicated genotypes. Representative confocal images are shown. Enhanced red fluorescence was detected in KO, brain-RE, and muscle-RE mice, as compared to WT and RE/RE mice. Quantification of oxidized (red) / unoxidized (green) ratio. Scale bars, 10 μm. Results are shown as mean ± SEM; **P* < 0.05; Box plot include 50% of data points; the line represents the median, and the whiskers extend to the maximum and minimum values. *****P* < 0.0001, ***P* < 0.001, **P* < 0.05, ns, non-significant.

Figure S6. Identification of feeding rhythm-dependent genes (A) Schematic outline of the time-restricted feeding (TRF) protocol used for WT, muscle-RE, or KO mice, as indicated. Young (9- to 10-week-old) mice were fed only during the active time (dark phase) for about 9 to 10 hours for TRF conditions. Muscle was collected after 16 weeks of either TRF or ad libitum feeding (ALF). No food was available for TRF during the rest time (light phase) during the entire experiment. (**B**) Abundance profiles of core clock genes in WT/ALF, muscle-RE/ALF, or muscle-RE/TRF mice. (**C**) Phase-sorted expression heatmap of 488 genes that oscillated only in WT/ALF or muscle-RE/TRF mice, but not in muscle-RE/ALF mice (dryR; WT/ALF, muscle-RE/ALF, muscle-RE/TRF, BICW ≥ 0.4, amp ≥ 0.25). (**D**) Density plot comparing 488 rhythmic genes amplitudes; Welch's t-test, WT/ALF versus muscle-RE/TRF, t = -2.28, *P* = 0.023. (E) Circular plots showing peak phase distribution of rhythmic core-clock genes oscillating in WT/ALF, muscle-RE/ALF, muscle-RE/TRF, KO/ALF, or KO/TRF mice at 26 weeks of age (JTK_CYCLE, adjusted *P* < 0.05). **(F**). Principal component analysis (PCA) of the full transcriptome of TA muscle from WT/TRF, muscle-RE/TRF, or KO/TRF mice (in 26-week-old mice). (**G**) Number

of TRF-driven genes classified in dryR models in WT/ALF, muscle-RE/ALF, muscle-RE/TRF, or RE/RE/ALF mice. Blue indicates rhythmic detection; white indicates no rhythms detected between samples. (**H**) Phase-sorted expression heatmap of 236 brain–muscle communication–dependent, TRF-driven genes that oscillated only in WT/ALF, RE:RE/ALF, and muscle-RE/TRF mice, but not in muscle-RE/ALF mice (dryR, BICW≥0.4, amp≥0.25). (**I**) Density plot comparing 236 rhythmic transcript amplitudes; Welch's t-test, WT/ALF versus muscle-RE/ALF, t = 8.45, p = 4.8E-16; WT/ALF versus muscle-RE/TRF, t = -1.75, p = 0.08 (not significant). WT versus RE:RE/ALF, t = -1.48, p = 0.14, (not significant). (**J**) Circular histogram plots of the peak phase (JTK_CYCLE) of 236 genes oscillating in WT/ALF, muscle-RE/TRF, and RE:RE/ALF mice. (**K**) Abundance profiles of the indicated genes in WT/ALF, muscle-RE/TRF, muscle-RE/ALF, and RE/RE/ALF. (**L, M**) Functional enrichment bubble plot showing selected gene sets; MSigDB canonical pathways, GOBP enrichment ($P < 0.05$) analysis of genes that were TRF/brain–muscle clock–driven (236 genes) or TRF/clock-driven (107 genes).

Figure S7. Effect of time-restricted feeding (TRF) on muscle physiology. (A) Quantification of collagen deposition by Sirius red staining, with the number of $eMHC^+$ fibers, and centrally nucleated fibers (CNFs) in tibialis anterior (TA) muscle from WT, KO, or muscle-RE mice under ALF or TRF conditions. (**B, C**) Representative images and quantification of in vivo MitoTimer reporter expression in myofibers of TA muscle of the indicated mice genotypes and treatments to assess mitochondria stress. Oxidized (red)/unoxidized (green) ratio was quantified. *$P < 0.05$, ***$P < 0.001$; ns, not significant. (**D**) Normalized food intake of each mouse genotype after 5 weeks of experiment and body weight at the end of the experiment. **E**) Metabolic parameters and activity patterns in young and aged mice after TRF, showing: left, locomotor activity pattern, and right, oxygen consumption and energy expenditure; and (**F**) lipid and glucose oxidation graph. (**G**) Survival curves of muscle-RE/ALF, muscle-RE/TRF, KO/ALF, and KO/TRF mice. (**H**) Representative H&E images and quantification of mean fiber size in TA muscle of WT, KO, and muscle-RE mice under an ALF or a TRF regime. (**I**) Force-frequency curves of EDL muscle of the different experimental groups at about 26-weeks of age. Scale bars, 50 μm. Data are represented as ± s.e.m. Force-frequency curves, two-way ANOVA; survival curve, Mantel-Cox test, compared to the same genotype under ALF. *$P < 0.05$, **$P < 0.01$, ***$P < 0.001$.

Figure S8. Muscle and brain clocks communication. (A, B) Measurements of corticosterone (glucocorticoids) at day/night (ZT0, ZT12) in indicated genotypes. Results as mean ± SEM; *$P < 0.05$; ns, **$P < 0.01$, non-significant. (**C**) Disruption of pathways through adrenalectomy (ADX), measurements of corticosterone (glucocorticoids) at day/night (ZT0, ZT12) in sham and ADX mice. Results as mean ± SEM; **$P < 0.01$. (**D**) Normalized food intake in sham or ADX mice. (**E, F**) Clock gene expression profile in WT and RE/RE, sham or bilateral ADX mice at ZT0 and ZT12.

Figure S9. Muscle and brain clock communication. (**A, B**). Expression profile of clock and the indicated genes in WT (wild-type) and RE/RE mice with sham surgery or bilateral adrenalectomy (ADX) at two time points, ZT0 (beginning of light phase) and ZT12 (beginning of dark phase). Mice were administered exogenous dexamethasone (Dex, a synthetic glucocorticoid) or adrenaline (Adr). (**C**). Functional enrichment bubble plot showing selected gene sets; MSigDB canonical pathways enrichment ($P < 0.05$) analysis of WT-ADX genes comparison to WT-sham. (**D**). Quantification of collagen content by Sirius red staining, fibers number of fibers expressing embryonic myosin, inflammatory phenotypes as presence of high infiltrating myeloid CD11b+ cells in tibialis anterior (TA) muscle. Results are mean ± s.e.m. $*P < 0.05$, $**P < 0.01$; (*t*-test; two-tailed).

Figure S10. Effect of time-restricted feeding (TRF) on physiologically aged mice. (**A**) Quantification of β2-adrenergic receptor (extracellular) and glucocorticoid receptor protein immunostaining in cryosections of tibialis anterior (TA) muscle from young (10- to 12-week-old [WO]) or old (>96-WO) mice. (**B**) Schematic overview of TRF used in this study for physiologically aged old mice. Old WT mice (66- to 74-WO) had TRF (i.e., food only for 9 to 10 hours during the active [night] phase) or ad libitum feeding (ALF) for ~26 weeks prior to muscle collection (endpoint, 92- to 116-WO mice). $n = 24$ mice for each group, with 4 mice (2 male, 2 females) at each timepoint. The comparison groups were young WT mice (10- to 12-WO) only with ALF, or with ALF followed by 16 weeks of TRF (young/TRF) (endpoint, 26- to 28-WO mice; as in Fig. 5A). (**C**) Abundance profiles of core clock genes in WT/ALF, old/ALF, or old/TRF under 12/12 hour light/dark (L/D) entrainment; $n = 3$ or 4 mice at each time point. Data are presented as mean ± SD. (**D**) Circular plots showing peak phase distribution of rhythmic core-clock genes oscillating in young WT/ALF, old/ALF, and old/TRF.

Figure S11. Feeding–fasting rhythms prevent physiological age-associated rhythmic reprogramming. (**A**) Differential rhythmicity analysis (dryR) of young (10- to 12-weeks old) WT/ALF, old/ALF, and old/TRF. Number of genes classified in dryR rhythmic models (BICW ≥ 0.4, amp ≥ 0.25). Blue indicates rhythmic detection; white indicates no rhythms detected between samples. (**B**) Phase-sorted expression heatmap of 452 genes that oscillated in WT/ALF, lost rhythm in old/ALF, and recovered in old/TRF mice (dryR; BICW ≥ 0.4, amp ≥ 0.25). (**C**) Circular histogram plots of the peak phase (JTK_CYCLE) of 452 rhythmic genes oscillating in WT/ALF and old/TRF mice. (**D**) Density plot showing rhythmic transcripts amplitude comparison for 452 genes; Welch's *t*-test, young WT/ALF versus old/TRF, $t = 0.35$, $P = 0.73$ (not significant). (**E**) Functional enrichment bubble plot showing selected gene sets; MSigDB canonical pathways, GOBP enrichment ($P < 0.05$) analysis of 452 genes. (**F**) Circular 24-hour phase distribution of aggregated muscle tissue-oriented functional categories in young/ALF,

old/ALF, and old/TRF WT mice (PSEA, Kuiper Q-value [vs. uniform] < 0.05). Young/ALF mice (see Fig. 3E) were re-used here for comparison.

Figure S12. Rhythmic alterations in physiologically aged mice. (**A**) Phase-sorted expression heatmap of 209 genes that oscillated only in old/ ALF, but not in young WT/ALF or old/TRF mice (dryR; WT/ALF, old/ALF, old/TRF, BICW≥0.4, amp≥0.25). (**B**) Functional enrichment bubble plot showing selected gene sets; MSigDB canonical pathways and hallmark enrichment ($P < 0.05$) analysis of 209 rhythmic genes gained in old/ALF. (**C**) Circular histogram plots of the peak phase (JTK_CYCLE) of 209 rhythmic genes that oscillating only in old/ALF mice. (**D**) Quantification of the activity patterns, energy expenditure, and lipid and glucose oxidation in mice of the different experimental groups Data are represented as mean ± s.e.m. Two-tailed *t*-test. *$P < 0.05$, **$P< 0.01$, ***$P < 0.001$.

Figure S13. Prevention of muscle aging through muscle–brain clock communication network. (**A**) Phase-sorted expression heatmap of 765 genes that commonly oscillated in RE/RE, muscle-RE/TRF and old/TRF using dryR rhythmic analysis (dryR; BICW ≥ 0.4, amp ≥ 0.25). (**B**) Circular histogram plots of the peak phase (JTK_CYCLE) distribution of 765 rhythmic genes in RE/RE, muscle-RE/TRF and old/TRF. (**C**) Density plot comparing 765 rhythmic genes amplitudes; Welch's *t*-test, RE/RE versus old/TRF t = -2.41, $P = 0.016$ (not significant). **(D)** Functional enrichment bubble plot showing selected gene sets; MSigDB canonical pathways, GOBP and hallmark enrichment ($P < 0.05$) analysis of 765 genes.

Supplementary table legends

Supplementary tables are available on Dryad https://doi.org/10.5061/dryad.8931zcrxp

Table S1. Rhythmic transcriptome output by JTK_CYCLE in defined mice genotypes, with 12:12 hour light/dark (LD) cycles.

Table S2. Rhythmic transcriptome output by RAIN in defined mice genotypes, with 12:12 hour LD cycles.

Table S3. Differential rhythmicity analysis dryR in defined mice genotypes, with 12:12 hour LD cycles.

Table S4. Transcription factor motif enrichment analysis using g:Profiler, with 12:12 hour LD cycles.

Supplementary Materials

Materials and Methods

Animals

Mice were bred and maintained at the animal facilities of the Barcelona Science Park in strict accordance with the Spanish and European Union regulations. All experimental protocols were approved by the Catalan Government, following applicable legislation and the guidelines of the Institutional Animal Care and Use Committee (IACUC) of the Barcelona Science Park.

Bmal1-stopFL mice were generated as described previously (*9, 10*). Experimental mice were: knock-out (KO) *Bmal1*$^{stopFL/stopFL}$, Cre$^{-/-}$; muscle-RE (Muscle-RE) *Bmal1*$^{stopFL/stopFL}$, *Hsa*-Cre$^{-/tg}$; suprachiasmatic nucleus-RE (brain-RE) *Bmal1*$^{stopFL/stopFL}$, *Syt10*-Cre$^{-/tg}$, and suprachiasmatic nucleus + muscle-RE (RE/RE) *Bmal1*$^{stopFL/stopFL}$, *Syt10*-cre$^{-/tg}$; *Hsa*-Cre$^{-/tg}$ and wild-type (WT) littermates. Both male and female mice were used; they were maintained in standard 12:12 hour light/dark (LD) photoperiods and fed *ad libitum* unless otherwise specified. All mice were used at an average age of 10 weeks (range 9 to 12) and 26 weeks (range 25 to 28), except physiologically aged mice, which were used at 85 to 116 weeks of age, as indicated.

Male and female littermates were used for lifespan, metabolic cages analysis, and RNA-seq experiments (with 2 each per time point, unless otherwise specified). Female mice were used for histological analysis, and male mice for all other experiments (i.e., body weight, food consumption and *ex vivo* EDL force measurements).

Time-restricted feeding

Mice under a time-restricted feeding (TRF) regime had free access to food for 9 to 10 hours during the active dark phase, from *zeitgeber* time (ZT)13/14 to ZT22/23 (with lights on at ZT0) from Monday to Friday, and for 7 to 8 hours, from ZT12 to ZT19/20, on the weekends. Mice were put on TRF starting at 10 weeks of age until 24 to 27 weeks of age, except for physiologically aged mice, which were subjected to approximately 26 weeks of TRF (starting at the age of 63 to 76 weeks, until the age of 85 to 107 weeks).

Indirect calorimetry and locomotor activity

To assess indirect calorimetry measurements, n = 3 to 7 mice per condition were used. Measurements of oxygen consumption (VO_2), CO_2 production (VCO_2), energy expenditure (EE), respiration exchange ratio (RER), glucose and lipid oxidation, and ambulation were performed using an indirect calorimetry system (Oxymax, Columbus Instruments). Mice were acclimatized for 1 to 2 days, after which data were recorded for 3 consecutive days.

Western blot

Total homogenates from gastrocnemius muscle were obtained in RIPA lysis buffer (50 mM Tris-HCl pH 8, 150 mM NaCl, 5 mM EDTA, 15 mM $MgCl_2$, and 1% NP-40), supplemented with protease and phosphatase inhibitors (Sigma Aldrich, Complete Mini; Sigma Aldrich, Phosphatase Inhibitor Cocktail 1 and Phosphatase Inhibitor Cocktail 2). Samples were lysed for 30 min on ice and centrifuged at 13,000 rpm for 15 min at 4ºC, and the supernatant was collected. Protein concentration was measured using the Bradford method (Protein Assay, Bio-Rad). About 30 to 60 µg protein from each sample were resolved on 4%-12% gels (BioRad) and transferred to nitrocellulose membranes, which were blocked with 5% instant non-fat milk in TBS-T (0.1% Tween-20, TBS) for 2 hours at room temperature. The following primary antibodies were used (diluted in 5% milk TBS-T) and incubated overnight at 4 ºC: anti-phosphorylated BMAL1 (Ser42) (Cell Signalling #13936), anti-BMAL1 (Abcam #93806), and monoclonal anti-α-tubulin antibody (Sigma-Aldrich, #T-6199). Following HRP-conjugated secondary antibody incubation (Jackson ImmunoResearch Donkey anti-rabbit IgG #711-001-003; Agilent Dako rabbit anti-mouse immunoglobulins/HRP, #P0260) for 1 hour at room temperature, blots were visualized with ChemiDoc MP (Biorad, ChemiDoc™ MP Imaging System #12003154).

Muscle force measurements

Ex vivo force measurements of EDL muscle were assessed as previously described (*57*). Briefly, muscle was dissected and immediately placed in Krebs–Ringer bicarbonate buffer solution, with 10 mM glucose, and continuously oxygenated. The tendinous ends of muscle were attached to a fixed clamp and the lever-arm of an Aurora Scientific Instruments 300B actuator/transducer system by a nylon thread. A stimulation frequency ranging from 1 to 200 Hz was used to determine the maximum isometric-tetanic force, taking this value from the plateau of the curve. Force was then normalized per muscle area to calculate the specific force (mN/mm^2).

Muscle electroporation

For *MitoTimer* gene transfection in TA muscle, *MitoTimer* plasmid (Addgene #52659) was purified using an Endrofree plasmid kit (Qiagen #12362) and dissolved in PBS (final concentration of 2.5 µg/ml). This solution (30 µl) was injected directly into the TA muscle of anesthetized animals. After injection, an electroporator (BTX™ ECM™ 830 Electroporation Generator, Fisher Scientific #450052) was used to apply 10 pulses of 20 ms per muscle (175 V/cm, 1 Hz).

Immunohistochemistry and immunofluorescence

Muscle samples were embedded in OCT solution (TissueTek #4583), frozen in isopentane cooled with liquid nitrogen, and stored at −80 °C until analysis. Muscle cryosections (10-µm thick) were collected and stained for hematoxylin & eosin (H&E) (Sigma-Aldrich, #HHS80 and #45235),

Sirius red (Sigma-Aldrich #365548), and Oil Red O (Sigma-Aldrich #O0625) staining. Muscle cryosections (10-µm thick) were cut longitudinally for MitoTimer positive fiber visualization.

For immunohistochemistry assays, unfixed muscle cryosections were examined by standard immunohistochemical procedures for the expression of myosin heavy chain (MHC) isoforms. The primary monoclonal antibodies used were: anti-myosin IIB (BF-F3) and anti-eMHC (F1.625) (Developmental Studies Hybridoma Bank), rabbit polyclonal anti-phospho-DRP1 (Ser616) (Cell Signaling #3455), rabbit monoclonal anti-phospho-AMPKalfa (Thr172) (40H9) (Cell Signaling #2535), rat monoclonal anti-LAMP-1 (1D4B) (Santa Cruz Biotechnology #sc-19992), mouse monoclonal anti-dystrophin (Sigma #D8168), rabbit polyclonal anti-laminin (Sigma #L9393), rabbit polyclonal anti-β2-adrenergic receptor (extracellular) antibody (Alomone Labs #AAR-016), and mouse monoclonal anti-glucocorticoid Receptor (Invitrogen #MA1-510). For CD11b immunofluorescence assays, sections were fixed with 4% PFA and incubated with anti-CD11b (eBioscience, #14-0112-85), and anti-laminin antibody (Sigma, #L9393). Secondary antibodies used were Alexa Fluor 488 goat anti-rat IgG (Invitrogen, A-11006), or goat anti-rabbit IgG (Invitrogen, A11036). Nuclei were stained with 4',6-diamidino-2-phenylindole (DAPI).

Adrenalectomy (Adx) experiments

Mice were anesthetized with 2% inhaled isoflurane, and a midline incision were done in the abdominal cavity. The fat attached to the adrenal glands was pulled out of the cavity; after dissection of the adrenal gland, the fat was returned to the cavity, and the skin was sewn. The contralateral adrenal gland was similarly removed after two days. To compensate for the aldosterone loss, 0.9% of saline supplemented with 1% glucose was provided. A sham-operated group was used as a control. Muscle samples were then taken from the animals after they had recovered for at least two weeks from the effects of the adrenalectomy and anesthesia. In order to treat Adx mice with exogenous hormones, an intraperitoneally (IP) injection of 5 mg/kg dexamethasone (Sigma # D1159) or 0.5 mg/kg adrenaline (Sigma #E4642) was given for 10 days at ZT12. Corticosterone detection was performed according to the manufacturer's instruction (Abcam# ab108821).

Microscopy and image analysis

Digital images were acquired using the Leica DMR600B microscope equipped with a DFC300FX camera for histochemical color pictures and a TCS SP8 MP microscope (Leica Microsystems) for fluorescence pictures; fiber type distribution, CSA, and percentage of muscle area positive for Sirius red and Oil red staining were quantified using Image J software. Images from *MitoTimer*-positive fibers were analyzed by quantifying the red:green ratio with Image J software.

RNA isolation and sequencing

Total RNA was extracted from the snap-frozen tibialis anterior (TA) muscle. Briefly, after homogenization with Qiazol reagent (Qiagen #1023537), RNA was isolated using miRNeasy Mini Kit (Qiagen #1038703); samples were then digested with DNase (Qiagen #1010395) according to the manufacturer's instructions.

RNA quality was checked using Nanodrop and RNA 6000 Nano Assay on a Bioanalyzer 2100 (Agilent). RNA-seq libraries were sequenced in paired-end mode with a read length of 150 base pairs with an average of 2 × 25 million reads for each sample. Four biological replicates (2 males and 2 females) at each ZT point were used to collect RNA samples. A total of 384 mouse RNA samples (24 mouse samples × 16 conditions) were sequenced to generate the total circadian RNA transcriptome. Additional 48 samples for adrenalectomy (Adx) experiments were sequenced for two time points (ZT0 and ZT12).

RNA-seq data processing

Sequencing reads were pre-processed using the nf-core/RNAseq pipeline (*85*), and read quality was assessed by FastQC (Table 1). TrimGalore (Table 1) was used to trim sequencing reads, eliminate Illumina adaptor remains, and discard short reads. The resulting reads were mapped onto the mouse genome (GRCm38, release 81; Table 1) using HiSAT2 (*86*) and quantified using featureCounts (*87*). Overall, 8 samples were removed due to quality issues: WT_10w_ALF_3.ZT0, WT_26w_ALF_12.ZT8, WT_26w_ALF_21.ZT20, brain-RE_10w_ALF_11.ZT8, brain-RE_26w_ALF_6.ZT4, brain-RE_26w_ALF_21.ZT20, KO_26w_TRF_7.ZT4 and KO_26w_TRF_20.ZT16. Variance-stabilizing transformation of raw count data was applied using Bioconductor package DEseq2 (*88*) to visualize the sample-to-sample distances in principal component analysis (PCA). Trimmed mean of M-values (TMM)-normalized fragments per kilobase per million mapped reads (FPKM) values were calculated using Bioconductor package edgeR (*89*) and log2-transformed with a pseudo count of 0.01. In each analysis performed, the expression datasets were adjusted for biological (sex) and technical (batch) effects. Overall, 14,413 genes with average non-transformed FPKM expression > 0.5 in at least one-time point of at least one experimental condition were considered for further analysis. The same filtering approach left 13,500 genes in additional adrenalectomy experiments, respectively.

Identification of rhythmic transcripts

Rhythmic transcripts were detected based on data from expression at six time points using the non-parametric Jonckheere-Terpstra-Kendall (JTK_CYCLE) algorithm (*31*), which detects cosine waveform and provides amplitude and phase output of rhythmic genes over a period of 20 to 24 hours. Genes with permutation-based P-value Bonferroni-adjusted for multiple testing ($P <$

0.05) were considered rhythmic over the circadian cycle (table S1). GraphPad Prism software (Table 1) was used to plot the abundance of most representative rhythmic genes. RAIN (rhythmicity analysis incorporating nonparametric methods) (*32*) was used as an additional rhythmic transcript detection method; it detects both symmetric and asymmetric waveforms of rhythmic genes over a period of 24 hours. Genes with Benjamini–Hochberg adjustment ($P < 0.01$) were considered rhythmic over the circadian cycle (table S2). The R package UpSetR (*90*) was used for a visual representation of rhythmic gene intersections between conditions for each method. GraphPad Prism software (Table 1) was used to plot the abundance of the most representative rhythmic transcripts, with ZT0 expression data duplicated to ZT24 for diurnal rhythmic visual representation. Heatmaps of the expression of the rhythmic transcript were plotted by R package pheatmap (Table 1). Amplitude density plots and phase histograms were generated using R package ggplot2 (Table 1). Circular plots showing peak phase distribution of core clock genes were made with R package circlize (*91*).

Differential rhythmicity analysis (dryR)

Differentially rhythmic categories corresponding to gain, loss or the same rhythm were defined using the "dryseq()" function of the R package dryR. The following filtering criteria were used to select genes with the expression rhythmic in a respective model: Bayesian information criterion weight (BICW) ≥ 0.4 and amplitude ≥ 0.25 (tables S3). Genes with maximal Cook's distance ≥ 1 across the replicates were considered as outliers and removed. Expression heatmaps for corresponding rhythmic genes were plotted by R package pheatmap (Table 1). Amplitude density plots and phase histograms were generated using R package ggplot2 (Table 1) for selected differentially rhythmic categories based on the output statistics from JTK_CYCLE.

Functional profiling of rhythmic transcriptome

Enrichment of MsigDB gene sets (GOBP, canonical pathways and hallmarks) was performed using a hypergeometric test employing "phyper()" function of stats R package with significance defined by Benjamini–Hochberg adjustment ($P < 0.05$). Functional enrichment results were visualized using the SRplot enrichment bubble plot tool (Table 1).

For functional characterization of the global rhythmic transcriptome in each condition, phase set enrichment analysis (PSEA) was performed with the following parameters: domain from 0 to 24 hours, minimum of 10 genes per gene set, and maximum 10,000 simulations. Output JTK CYCLE files containing the list of cycling genes and their peak phases of expression were used as input. Tests were run separately for Molecular Signatures Database (MSigDB) gene ontology biological processes (GOBP) and canonical pathways (KEGG and Reactome) gene sets (83). Enrichment was tested against a uniform background distribution to summarize any overall synchronization of peak phases within gene sets. A Kuiper Q value < 0.05 was used as a significance threshold. R

package circlize (84) was used to plot rhythmic functions on a temporal scale. A semi-automated approach was applied to aggregate individual gene sets into broad muscle tissue-oriented functional categories based on semantic similarity, positions in hierarchical trees of corresponding databases, and the analysis of gene set descriptions. This allowed the peak phases distributions (vector-average values) to be obtained within the main rhythmic functions, and their span and temporal synchronization to be visualized across the diurnal cycle.

Identification of transcripts that oscillate between ZT0 and ZT12

Oscillation of transcripts between the ZT0 and ZT12 time points in the Adx dataset was studied using differential expression analysis with the Bioconductor package limma (*92*). The "voomWithQualityWeights()" function was used to transform read counts, default parameters for fitting linear model, and empirical Bayes moderation for standard errors. Genes with adjusted $P < 0.05$ were considered as differentially expressed. R package ggplot2 was used to plot the abundance of most representative oscillating transcripts, with ZT0 expression data being duplicated to ZT24 for diurnal rhythm visual representation.

Functional profiling of transcripts oscillating between ZT0 and ZT12

The GSEA software (Broad Institute) was used to functionally characterize gene expression oscillations observed in the two–time point data sets. Enrichment of MsigDB gene sets (GOBP, canonical pathways, and hallmarks) was performed using the following specific parameters: "gene_set" permutation type, "RatioOfClasses" metric for ranking genes with median for class metrics instead of mean. A FDR q-value threshold 0.25 was used to delineate significant gene set enrichment.

Statistics

For mouse experiments, no specific blinding method was used, but mice in each sample group were selected randomly. The sample size (n) of each experimental group is described in each corresponding figure legend. GraphPad Prism software was used for all statistical analyses. Quantitative data displayed as histograms are expressed as means ± standard error of the mean (represented as error bars), and results from each group were averaged and used to calculate descriptive statistics. For each experiment, statistical tests and significance thresholds are provided in each figure legend.

Table 1: Software and algorithm details

circlize v0.4.9	Z. Gu, L. Gu, R. Eils, M. Schlesner, B. Brors. circlize implements and enhances circular	https://cran.r-project.org/package=circlize

	visualization in R. *Bioinformatics*. 30 (2014), pp.2811-2812	
DESeq2 v1.28.1	M.I. Love, W. Huber, S. Anders. Moderated estimation of fold change and dispersion for RNA-seq data with DESeq2. *Genome Biol.*, 15 (2014), p. 550	http://bioconductor.org/packages/release/bioc/html/DESeq2.html
edgeR v3.30.0	M.D. Robinson, D.J. McCarthy, G.K. Smyth. edgeR: a Bioconductor package for differential expression analysis of digital gene expression data. *Bioinformatics*, 26 (2009), pp. 139–140	http://bioconductor.org/packages/release/bioc/html/edgeR.html
Ensembl GRCm38, release 81	F. Cunningham *et al.* Ensembl 2015. *Nucleic Acids Res.*, 43 (2015), pp. D662–D669	ftp://ftp.ensembl.org/pub/release-81/
Gene ontology	M. Ashburner *et al.* Gene ontology: tool for the unification of biology. The Gene Ontology Consortium. *Nat. Genet*, 25 (2000), pp. 25-29 The Gene Ontology Consortium. The Gene Ontology Resource: 20 years and still GOing strong. *Nucleic Acids Res*., 47 (2019), pp. D330-D338	http://geneontology.org/
FastQC v0.11.8	S. Andrews. FastQC: a quality control tool for high throughput sequence data. (2010), Cambridge, UK	https://www.bioinformatics.babraham.ac.uk/projects/fastqc/
featureCounts v1.6.2	Y. Liao, G.K. Smyth, W. Shi. featureCounts: an efficient general purpose program for assigning sequence reads to genomic features. *Bioinformatics*, 30 (2014), pp. 923-930	http://bioinf.wehi.edu.au/featureCounts/
ggplot2 v3.3.0	H. Wickham. ggplot2: Elegant graphics for data analysis. (2016)	https://cran.r-project.org/package=ggplot2
gprofiler2 v0.1.9	U. Raudvere, L. Kolberg, I. Kuzmin, T. Arak, P. Adler, H. Peterson, J. Vilo. g:Profiler: a web server for functional enrichment analysis and	https://cran.r-project.org/package=gprofiler2

	conversions of gene lists (2019 update). *Nucleic Acids Res*., 47 (2019), pp. W191–W198	
GraphPad Prism v6.0C	GraphPad Software, San Diego, California USA	www.graphpad.com
HiSAT2 v2.1.0	D. Kim, J.M. Paggi, C. Park, C. Bennett, S.L. Salzberg. Graph-based genome alignment and genotyping with HISAT2 and HISAT-genotype. *Nat. Biotechnol*, 37 (2019), pp. 907–915	https://daehwankimlab.github.io/hisat2/
JTK_CYCLE v3.1p	M.E. Hughes, J.B. Hogenesch, K. Kornacker. JTK_CYCLE: an efficient nonparametric algorithm for detecting rhythmic components in genome-scale data sets. *J Biol Rhythms*, 25 (2010), pp. 372-380	https://github.com/gangwug/MetaCycle/blob/master/R/JTKv3.1p.R
KEGG	M. Kanehisa, S. Goto. KEGG: Kyoto Encyclopedia of Genes and Genomes. *Nucleic Acids Res.,* 28 (2000), pp. 27-30	https://www.genome.jp/kegg/pathway.html
limma v3.44.1	M.E. Ritchie, B. Phipson, D. Wu, Y. Hu, C.W. Law, W. Shi, G.K Smyth. limma powers differential expression analyses for RNA-sequencing and microarray studies. *Nucleic Acids Res.*, 43 (2015), e47.	https://bioconductor.org/packages/release/bioc/html/limma.html
MSigDB v7.2	A. Liberzon et al. Molecular signatures database (MSigDB) 3.0. *Bioinformatics*, 27 (2011), pp. 1739–1740	https://www.gsea-msigdb.org/gsea/msigdb
nf-core/rnaseq v1.2	P.Ewels, A. Peltzer, S. Fillinger, H. Patel, J. Alneberg, A. Wilm, M. Ulysse Garcia, P. Di Tommaso, S. Nahnsen. The nf-core framework for community-curated bioinformatics pipelines. *Nat. Biotechnol*, 38 (2020), pp. 276–278	https://github.com/nf-core/rnaseq

pheatmap v1.0.12	R. Kolde. pheatmap: Pretty heatmaps Software. (2015)	https://cran.r-project.org/package=pheatmap
PSEA v1.1	R. Zhang, A.A. Podtelezhnikov, J.B. Hogenesch, R.C. Anafi. Discovering biology in periodic data through Phase Set Enrichment Analysis (PSEA). *J Biol Rhythms*. 31 (2016), pp. 244-257	https://github.com/ranafi/PSEA
R v4.0.0	R Core Team. R: A language and environment for statistical computing. R Foundation for Statistical Computing. (2014), Vienna, Austria	https://www.r-project.org/
rain v1.22.0	P.F. Thaben, P.O. Westermark. Detecting Rhythms in Time Series with RAIN. *J Biol Rhythms*, 29 (2014), pp. 391–400	https://bioconductor.org/packages/release/bioc/html/rain.html
Reactome	B. Jassal *et al.* The reactome pathway knowledgebase. *Nucleic Acids Res.*, 48 (2020), pp. D498-D503	https://reactome.org/
Trim Galore! v0.5.0	F. Krueger. Trim Galore! (2012), Cambridge, UK	https://www.bioinformatics.babraham.ac.uk/projects/trim_galore/

References and notes

1. J. Bass, M. A. Lazar, Circadian time signatures of fitness and disease. *Science (1979)* **354**, 994–999 (2016).
2. S. Panda, Circadian physiology of metabolism. *Science (1979)* **354**, 1008–1015 (2016).
3. J. S. Takahashi, Transcriptional architecture of the mammalian circadian clock. *Nat Rev Genet* **18**, 164–179 (2017).
4. J. A. Mohawk, C. B. Green, J. S. Takahashi, Central and peripheral circadian clocks in mammals. *Annu Rev Neurosci* **35**, 445–462 (2012).
5. E. D. Herzog, T. Hermanstyne, N. J. Smyllie, M. H. Hastings, Regulating the suprachiasmatic nucleus (SCN) circadian clockwork: Interplay between cell-autonomous and circuit-level mechanisms. *Cold Spring Harb Perspect Biol* **9** (2017).
6. K. B. Koronowski, P. Sassone-Corsi, Communicating clocks shape circadian homeostasis. *Science* **371**, eabd0951 (2021).

7. D. Guan, Y. Xiong, T. M. Trinh, Y. Xiao, W. Hu, C. Jiang, P. Dierickx, C. Jang, J. D. Rabinowitz, M. A. Lazar, The hepatocyte clock and feeding control chronophysiology of multiple liver cell types. *Science (1979)* **369**, 1388–1395 (2020).
8. A. Easton, P. Meerlo, B. Bergmann, F. W. Turek, The suprachiasmatic nucleus regulates sleep timing and amount in mice. *Sleep* **27**, 1307–1318 (2004).
9. K. B. Koronowski, K. Kinouchi, P. S. Welz, J. G. Smith, V. M. Zinna, J. Shi, M. Samad, S. Chen, C. N. Magnan, J. M. Kinchen, W. Li, P. Baldi, S. A. Benitah, P. Sassone-Corsi, Defining the Independence of the Liver Circadian Clock. *Cell* **177**, 1448-1462.e14 (2019).
10. P. S. Welz, V. M. Zinna, A. Symeonidi, K. B. Koronowski, K. Kinouchi, J. G. Smith, I. M. Guillén, A. Castellanos, G. Crainiciuc, N. Prats, J. M. Caballero, A. Hidalgo, P. Sassone-Corsi, S. A. Benitah, BMAL1-Driven Tissue Clocks Respond Independently to Light to Maintain Homeostasis. *Cell* **177**, 1436-1447.e12 (2019).
11. J. G. Smith, K. B. Koronowski, T. Mortimer, T. Sato, C. M. Greco, P. Petrus, A. Verlande, S. Chen, M. Samad, E. Deyneka, L. Mathur, R. Blazev, J. Molendijk, A. Kumar, O. Deryagin, M. Vaca-Dempere, V. Sica, P. Liu, V. Orlando, B. L. Parker, P. Baldi, P. S. Welz, C. Jang, S. Masri, S. A. Benitah, P. Muñoz-Cánoves, P. Sassone-Corsi, Liver and muscle circadian clocks cooperate to support glucose tolerance in mice. *Cell Rep* **42** (2023).
12. J. G. Smith, J. Molendijk, R. Blazev, W. H. Chen, Q. Zhang, C. Litwin, V. M. Zinna, P.-S. Welz, S. A. Benitah, C. M. Greco, P. Sassone-Corsi, P. Muñoz-Cánoves, B. L. Parker, K. B. Koronowski, Impact of Bmal1 Rescue and Time-Restricted Feeding on Liver and Muscle Proteomes During the Active Phase in Mice. *Molecular & Cellular Proteomics* **22**, 100655 (2023).
13. K. A. Dyar, D. Lutter, A. Artati, N. J. Ceglia, Y. Liu, D. Armenta, M. Jastroch, S. Schneider, S. de Mateo, M. Cervantes, S. Abbondante, P. Tognini, R. Orozco-Solis, K. Kinouchi, C. Wang, R. Swerdloff, S. Nadeef, S. Masri, P. Magistretti, V. Orlando, E. Borrelli, N. H. Uhlenhaut, P. Baldi, J. Adamski, M. H. Tschöp, K. Eckel-Mahan, P. Sassone-Corsi, Atlas of Circadian Metabolism Reveals System-wide Coordination and Communication between Clocks. *Cell* **174**, 1571-1585.e11 (2018).
14. G. Manella, E. Sabath, R. Aviram, V. Dandavate, S. Ezagouri, M. Golik, Y. Adamovich, G. Asher, The liver-clock coordinates rhythmicity of peripheral tissues in response to feeding. *Nat Metab* **3**, 829–842 (2021).
15. M. Bonaconsa, G. Malpeli, A. Montaruli, F. Carandente, G. Grassi-Zucconi, M. Bentivoglio, Differential modulation of clock gene expression in the suprachiasmatic nucleus, liver and heart of aged mice. *Exp Gerontol* **55**, 70–79 (2014).
16. S. Farajnia, S. Michel, T. Deboer, H. T. van der Leest, T. Houben, J. H. T. Rohling, A. Ramkisoensing, R. Yasenkov, J. H. Meijer, Evidence for neuronal desynchrony in the aged suprachiasmatic nucleus clock. *Journal of Neuroscience* **32**, 5891–5899 (2012).
17. T. J. Nakamura, N. N. Takasu, W. Nakamura, The suprachiasmatic nucleus: age-related decline in biological rhythms. *Journal of Physiological Sciences* **66**, 367–374 (2016).

18. T. J. Nakamura, W. Nakamura, S. Yamazaki, T. Kudo, T. Cutler, C. S. Colwell, G. D. Block, Age-related decline in circadian output. *Journal of Neuroscience* **31**, 10201–10205 (2011).
19. S. Sato, G. Solanas, F. O. Peixoto, L. Bee, A. Symeonidi, M. S. Schmidt, C. Brenner, S. Masri, S. A. Benitah, P. Sassone-Corsi, Circadian Reprogramming in the Liver Identifies Metabolic Pathways of Aging. *Cell* **170**, 664-677.e11 (2017).
20. G. Solanas, F. O. Peixoto, E. Perdiguero, M. Jardí, V. Ruiz-Bonilla, D. Datta, A. Symeonidi, A. Castellanos, P. S. Welz, J. M. Caballero, P. Sassone-Corsi, P. Muñoz-Cánoves, S. A. Benitah, Aged Stem Cells Reprogram Their Daily Rhythmic Functions to Adapt to Stress. *Cell* **170**, 678-692.e20 (2017).
21. L. García-Prat, M. Martínez-Vicente, E. Perdiguero, L. Ortet, J. Rodríguez-Ubreva, E. Rebollo, V. Ruiz-Bonilla, S. Gutarra, E. Ballestar, A. L. Serrano, M. Sandri, P. Muñoz-Cánoves, Autophagy maintains stemness by preventing senescence. *Nature* **529**, 37–42 (2016).
22. J. Segalés, E. Perdiguero, A. L. Serrano, P. Sousa-Victor, L. Ortet, M. Jardí, A. V. Budanov, L. Garcia-Prat, M. Sandri, D. M. Thomson, M. Karin, J. Hee Lee, P. Muñoz-Cánoves, Sestrin prevents atrophy of disused and aging muscles by integrating anabolic and catabolic signals. *Nat Commun* **11**, 1–13 (2020).
23. S. A. Benitah, P. S. Welz, Circadian Regulation of Adult Stem Cell Homeostasis and Aging. *Cell Stem Cell* **26**, 817–831 (2020).
24. V. A. Acosta-Rodríguez, F. Rijo-Ferreira, C. B. Green, J. S. Takahashi, Importance of circadian timing for aging and longevity. *Nat Commun* **12** (2021).
25. R. V. Kondratov, A. A. Kondratova, V. Y. Gorbacheva, O. V. Vykhovanets, M. P. Antoch, Early aging and age-related pathologies in mice deficient in BMAL1, the core component of the circadian clock. *Genes Dev* **20**, 1868–1873 (2006).
26. S. Schiaffino, B. Blaauw, K. A. Dyar, The functional significance of the skeletal muscle clock: Lessons from Bmal1 knockout models. *Skelet Muscle* **6**, 1–9 (2016).
27. K. A. Dyar, S. Ciciliot, L. E. Wright, R. S. Biensø, G. M. Tagliazucchi, V. R. Patel, M. Forcato, M. I. P. Paz, A. Gudiksen, F. Solagna, M. Albiero, I. Moretti, K. L. Eckel-Mahan, P. Baldi, P. Sassone-Corsi, R. Rizzuto, S. Bicciato, H. Pilegaard, B. Blaauw, S. Schiaffino, Muscle insulin sensitivity and glucose metabolism are controlled by the intrinsic muscle clock. *Mol Metab* **3**, 29–41 (2014).
28. G. Yang, L. Chen, G. R. Grant, G. Paschos, W. L. Song, E. S. Musiek, V. Lee, S. C. McLoughlin, T. Grosser, G. Cotsarelis, G. A. Fitzgerald, Timing of expression of the core clock gene Bmal1 influences its effects on aging and survival. *Sci Transl Med* **8** (2016).
29. J. Wefers, D. Van Moorsel, J. Hansen, N. J. Connell, B. Havekes, J. Hoeks, W. D. Van Marken Lichtenbelt, H. Duez, E. Phielix, A. Kalsbeek, M. V. Boekschoten, G. J. Hooiveld, M. K. C. Hesselink, S. Kersten, B. Staels, F. A. J. L. Scheer, P. Schrauwen, Circadian misalignment induces fatty acid metabolism gene profiles and compromises insulin sensitivity in human skeletal muscle. *Proc Natl Acad Sci U S A* **115**, 7789–7794 (2018).
30. P. Petrus, J. G. Smith, K. B. Koronowski, S. Chen, T. Sato, C. M. Greco, T. Mortimer, P.-S. Welz, V. Zinna, K. Shimaji, M. Cervantes, P. Baldi, P. Muñoz-Cánoves, P. Sassone-Corsi, S. A. Benitah, The central clock suffices to drive the

majority of circulatory metabolic rhythms. *bioRxiv* **2896**, 2022.01.24.477514 (2022).
31. M. E. Hughes, J. B. Hogenesch, K. Kornacker, JTK-CYCLE: An efficient nonparametric algorithm for detecting rhythmic components in genome-scale data sets. *J Biol Rhythms* **25**, 372–380 (2010).
32. P. F. Thaben, P. O. Westermark, Detecting rhythms in time series with rain. *J Biol Rhythms* **29**, 391–400 (2014).
33. B. D. Weger, C. Gobet, F. P. A. David, F. Atger, E. Martin, N. E. Phillips, A. Charpagne, M. Weger, F. Naef, F. Gachon, Systematic analysis of differential rhythmic liver gene expression mediated by the circadian clock and feeding rhythms. *Proc Natl Acad Sci U S A* **118** (2021).
34. R. Sartori, V. Romanello, M. Sandri, Mechanisms of muscle atrophy and hypertrophy: implications in health and disease. *Nat Commun* **12**, 1–12 (2021).
35. M. Buckingham, Skeletal muscle formation in vertebrates. *Curr Opin Genet Dev* **11**, 440–8 (2001).
36. C. Nelke, R. Dziewas, J. Minnerup, S. G. Meuth, T. Ruck, Skeletal muscle as potential central link between sarcopenia and immune senescence. *EBioMedicine* **49**, 381–388 (2019).
37. J. G. Tidball, I. Flores, S. S. Welc, M. Wehling-Henricks, E. Ochi, Aging of the immune system and impaired muscle regeneration: A failure of immunomodulation of adult myogenesis. *Exp Gerontol* **145**, 111200 (2021).
38. F. F. Bloise, A. Cordeiro, T. M. Ortiga-Carvalho, Role of thyroid hormone in skeletal muscle physiology. *J Endocrinol* **236**, R57–R68 (2018).
39. S. A. Brown, M. Sato, Marching to another clock. *Science (1979)* **367**, 740–741 (2020).
40. E. Ness-Cohn, R. Allada, R. Braun, Circadian rhythms in the absence of the clock gene Bmal1. *Science* **372**, 800–806 (2021).
41. R. Zhang, A. A. Podtelezhnikov, J. B. Hogenesch, R. C. Anafi, Discovering Biology in Periodic Data through Phase Set Enrichment Analysis (PSEA). *J Biol Rhythms* **31**, 244–257 (2016).
42. R. V. Kondratov, R. K. Shamanna, A. A. Kondratova, V. Y. Gorbacheva, M. P. Antoch, Dual role of the CLOCK/BMAL1 circadian complex in transcriptional regulation. *The FASEB Journal* **20**, 530–532 (2006).
43. D. van Moorsel, J. Hansen, B. Havekes, F. A. J. L. Scheer, J. A. Jörgensen, J. Hoeks, V. B. Schrauwen-Hinderling, H. Duez, P. Lefebvre, N. C. Schaper, M. K. C. Hesselink, B. Staels, P. Schrauwen, Demonstration of a day-night rhythm in human skeletal muscle oxidative capacity. *Mol Metab* **5**, 635–645 (2016).
44. J. A. Mayr, Lipid metabolism in mitochondrial membranes. *J Inherit Metab Dis* **38**, 137–144 (2015).
45. S. Shimba, N. Ishii, Y. Ohta, T. Ohno, Y. Watabe, M. Hayashi, T. Wada, T. Aoyagi, M. Tezuka, Brain and muscle Arnt-like protein-1 (BMAL1), a component of the molecular clock, regulates adipogenesis. *Proc Natl Acad Sci U S A* **102**, 12071–6 (2005).
46. S. Shimba, T. Ogawa, S. Hitosugi, Y. Ichihashi, Y. Nakadaira, M. Kobayashi, M. Tezuka, Y. Kosuge, K. Ishige, Y. Ito, K. Komiyama, Y. Okamatsu-Ogura, K. Kimura, M. Saito, Deficient of a clock gene, brain and muscle arnt-like protein-1

(BMAL1), induces dyslipidemia and ectopic fat formation. *PLoS One* **6**, 1–10 (2011).
47. D. A. Hood, J. M. Memme, A. N. Oliveira, M. Triolo, Maintenance of Skeletal Muscle Mitochondria in Health, Exercise, and Aging. *Annu Rev Physiol* **81**, 19–41 (2019).
48. S. Hood, S. Amir, The aging clock: circadian rhythms and later life. *J Clin Invest* **127**, 437–446 (2017).
49. S. Rath, R. Sharma, R. Gupta, T. Ast, C. Chan, T. J. Durham, R. P. Goodman, Z. Grabarek, M. E. Haas, W. H. W. Hung, P. R. Joshi, A. A. Jourdain, S. H. Kim, A. V Kotrys, S. S. Lam, J. G. McCoy, J. D. Meisel, M. Miranda, A. Panda, A. Patgiri, R. Rogers, S. Sadre, H. Shah, O. S. Skinner, T.-L. To, M. A. Walker, H. Wang, P. S. Ward, J. Wengrod, C.-C. Yuan, S. E. Calvo, V. K. Mootha, MitoCarta3.0: an updated mitochondrial proteome now with sub-organelle localization and pathway annotations. *Nucleic Acids Res* **49**, D1541–D1547 (2021).
50. L. Sardon Puig, M. Valera-Alberni, C. Canto, N. J. Pillon, Circadian Rhythms and Mitochondria: Connecting the Dots. *Front Genet* **9**, 452 (2018).
51. J. D. Wikstrom, T. Israeli, E. Bachar-Wikstrom, A. Swisa, Y. Ariav, M. Waiss, D. Kaganovich, Y. Dor, E. Cerasi, G. Leibowitz, AMPK regulates ER morphology and function in stressed pancreatic beta-cells via phosphorylation of DRP1. *Mol Endocrinol* **27**, 1706–1723 (2013).
52. E. Q. Toyama, S. Herzig, J. Courchet, T. L. Lewis Jr., O. C. Loson, K. Hellberg, N. P. Young, H. Chen, F. Polleux, D. C. Chan, R. J. Shaw, Metabolism. AMP-activated protein kinase mediates mitochondrial fission in response to energy stress. *Science (1979)* **351**, 275–281 (2016).
53. R. C. Laker, P. Xu, K. A. Ryall, A. Sujkowski, B. M. Kenwood, K. H. Chain, M. Zhang, M. A. Royal, K. L. Hoehn, M. Driscoll, P. N. Adler, R. J. Wessells, J. J. Saucerman, Z. Yan, A novel MitoTimer reporter gene for mitochondrial content, structure, stress, and damage in vivo. *J Biol Chem* **289**, 12005–12015 (2014).
54. E. Ferri, E. Marzetti, R. Calvani, A. Picca, M. Cesari, B. Arosio, Role of Age-Related Mitochondrial Dysfunction in Sarcopenia. *Int J Mol Sci* **21**, 5236 (2020).
55. E. Migliavacca, S. K. H. Tay, H. P. Patel, T. Sonntag, G. Civiletto, C. McFarlane, T. Forrester, S. J. Barton, M. K. Leow, E. Antoun, A. Charpagne, Y. Seng Chong, P. Descombes, L. Feng, P. Francis-Emmanuel, E. S. Garratt, M. P. Giner, C. O. Green, S. Karaz, N. Kothandaraman, J. Marquis, S. Metairon, S. Moco, G. Nelson, S. Ngo, T. Pleasants, F. Raymond, A. A. Sayer, C. Ming Sim, J. Slater-Jefferies, H. E. Syddall, P. Fang Tan, P. Titcombe, C. Vaz, L. D. Westbury, G. Wong, W. Yonghui, C. Cooper, A. Sheppard, K. M. Godfrey, K. A. Lillycrop, N. Karnani, J. N. Feige, Mitochondrial oxidative capacity and NAD(+) biosynthesis are reduced in human sarcopenia across ethnicities. *Nat Commun* **10**, 5808 (2019).
56. F. Damiola, N. Le Minh, N. Preitner, B. Kornmann, F. Fleury-Olela, U. Schibler, Restricted feeding uncouples circadian oscillators in peripheral tissues from the central pacemaker in the suprachiasmatic nucleus. *Genes Dev* **14**, 2950–2961 (2000).
57. B. J. Greenwell, A. J. Trott, J. R. Beytebiere, S. Pao, A. Bosley, E. Beach, P. Finegan, C. Hernandez, J. S. Menet, Rhythmic Food Intake Drives Rhythmic Gene Expression More Potently than the Hepatic Circadian Clock in Mice. *Cell Rep* **27**, 649-657.e5 (2019).

58. C. M. Greco, K. B. Koronowski, J. G. Smith, J. Shi, P. Kunderfranco, R. Carriero, S. Chen, M. Samad, P.-S. Welz, V. M. Zinna, T. Mortimer, S. K. Chun, K. Shimaji, T. Sato, P. Petrus, A. Kumar, M. Vaca-Dempere, O. Deryagin, C. Van, J. M. M. Kuhn, D. Lutter, M. M. Seldin, S. Masri, W. Li, P. Baldi, K. A. Dyar, P. Muñoz-Cánoves, S. A. Benitah, P. Sassone-Corsi, Integration of feeding behavior by the liver circadian clock reveals network dependency of metabolic rhythms. *Sci Adv* **7**, eabi7828–eabi7828 (2021).
59. L. Harder, H. Oster, The Tissue Clock Network: Driver and Gatekeeper of Circadian Physiology. *BioEssays* **42**, 1900158 (2020).
60. K.-A. Stokkan, Entrainment of the Circadian Clock in the Liver by Feeding. *Science (1979)* **291**, 490–493 (2001).
61. B. A. Hodge, X. Zhang, M. A. Gutierrez-Monreal, Y. Cao, D. W. Hammers, Z. Yao, C. A. Wolff, P. Du, D. Kemler, A. R. Judge, K. A. Esser, MYOD1 functions as a clock amplifier as well as a critical co-factor for downstream circadian gene expression in muscle. *Elife* **8** (2019).
62. A. Leliavski, R. Dumbell, V. Ott, H. Oster, Adrenal clocks and the role of adrenal hormones in the regulation of circadian physiology. *J Biol Rhythms* **30**, 20–34 (2015).
63. R. Dumbell, O. Matveeva, H. Oster, Circadian Clocks, Stress, and Immunity. *Front Endocrinol (Lausanne)* **7**, 37 (2016).
64. M. Soták, J. Bryndová, P. Ergang, K. Vagnerová, P. Kvapilová, M. Vodička, J. Pácha, A. Sumová, Peripheral circadian clocks are diversely affected by adrenalectomy. *Chronobiol Int* **33**, 520–529 (2016).
65. M. Surjit, K. P. Ganti, A. Mukherji, T. Ye, G. Hua, D. Metzger, M. Li, P. Chambon, Widespread negative response elements mediate direct repression by agonist-liganded glucocorticoid receptor. *Cell* **145**, 224–241 (2011).
66. A. M. Curtis, Y. Cheng, S. Kapoor, D. Reilly, T. S. Price, G. A. Fitzgerald, Circadian variation of blood pressure and the vascular response to asynchronous stress. *Proc Natl Acad Sci U S A* **104**, 3450–3455 (2007).
67. V. S. Ayyar, S. Sukumaran, Circadian rhythms: influence on physiology, pharmacology, and therapeutic interventions. *J Pharmacokinet Pharmacodyn* **48**, 321–338 (2021).
68. H.-C. Chang, L. Guarente, SIRT1 mediates central circadian control in the SCN by a mechanism that decays with aging. *Cell* **153**, 1448–1460 (2013).
69. M. Nygård, R. H. Hill, M. A. Wikström, K. Kristensson, Age-related changes in electrophysiological properties of the mouse suprachiasmatic nucleus in vitro. *Brain Res Bull* **65**, 149–154 (2005).
70. M. Sandri, L. Barberi, A. Y. Bijlsma, B. Blaauw, K. A. Dyar, G. Milan, C. Mammucari, C. G. Meskers, G. Pallafacchina, A. Paoli, D. Pion, M. Roceri, V. Romanello, A. L. Serrano, L. Toniolo, L. Larsson, A. B. Maier, P. Munoz-Canoves, A. Musaro, M. Pende, C. Reggiani, R. Rizzuto, S. Schiaffino, Signalling pathways regulating muscle mass in ageing skeletal muscle: the role of the IGF1-Akt-mTOR-FoxO pathway. *Biogerontology* **14**, 303–323 (2013).
71. V. Acosta-Rodríguez, F. Rijo-Ferreira, M. Izumo, P. Xu, M. Wight-Carter, C. B. Green, J. S. Takahashi, Circadian alignment of early onset caloric restriction promotes longevity in male C57BL/6J mice. *Science (1979)* **376**, 1192–1202 (2022).

72. A. Vainshtein, M. Sandri, Signaling pathways that control muscle mass. *Int J Mol Sci* **21**, 1–32 (2020).
73. C. López-Otín, G. Kroemer, Hallmarks of Health. *Cell* **184**, 33–63 (2021).
74. C. López-Otín, M. A. Blasco, L. Partridge, M. Serrano, G. Kroemer, Hallmarks of aging: An expanding universe. *Cell*, doi: 10.1016/j.cell.2022.11.001 (2023).
75. L. V. M. de Assis, H. Oster, The circadian clock and metabolic homeostasis: entangled networks. *Cellular and Molecular Life Sciences* **78**, 4563–4587 (2021).
76. E. M. Gibson, W. P. Williams 3rd, L. J. Kriegsfeld, Aging in the circadian system: considerations for health, disease prevention and longevity. *Exp Gerontol* **44**, 51–56 (2009).
77. S. Yamazaki, M. Straume, H. Tei, Y. Sakaki, M. Menaker, G. D. Block, Effects of aging on central and peripheral mammalian clocks. *Proc Natl Acad Sci U S A* **99**, 10801–10806 (2002).
78. A. A. Kondratova, R. V Kondratov, The circadian clock and pathology of the ageing brain. *Nat Rev Neurosci* **13**, 325–335 (2012).
79. M. A. Hofman, D. F. Swaab, Living by the clock: the circadian pacemaker in older people. *Ageing Res Rev* **5**, 33–51 (2006).
80. B. Roozendaal, W. A. van Gool, D. F. Swaab, J. E. Hoogendijk, M. Mirmiran, Changes in vasopressin cells of the rat suprachiasmatic nucleus with aging. *Brain Res* **409**, 259–264 (1987).
81. A. Chaudhari, R. Gupta, K. Makwana, R. Kondratov, Circadian clocks, diets and aging. *Nutr Healthy Aging* **4**, 101–112 (2017).
82. M. T. Sellix, J. A. Evans, T. L. Leise, O. Castanon-Cervantes, D. D. Hill, P. DeLisser, G. D. Block, M. Menaker, A. J. Davidson, Aging differentially affects the re-entrainment response of central and peripheral circadian oscillators. *Journal of Neuroscience* **32**, 16193–16202 (2012).
83. B. He, Z. Chen, Molecular Targets for Small-Molecule Modulators of Circadian Clocks. *Curr Drug Metab* **17**, 503–512 (2016).
84. O. Froy, Circadian rhythms, nutrition and implications for longevity in urban environments. *Proceedings of the Nutrition Society* **77**, 216–222 (2017).
85. F. Baylis, The nf-core framework for community-curated bioinformatics pipelines. *Nat Biotechnol* **38**, 271 (2020).
86. D. Kim, J. M. Paggi, C. Park, C. Bennett, S. L. Salzberg, Graph-based genome alignment and genotyping with HISAT2 and HISAT-genotype. *Nat Biotechnol* **37**, 907–915 (2019).
87. Y. Liao, G. K. Smyth, W. Shi, FeatureCounts: An efficient general purpose program for assigning sequence reads to genomic features. *Bioinformatics* **30**, 923–930 (2014).
88. M. I. Love, W. Huber, S. Anders, Moderated estimation of fold change and dispersion for RNA-seq data with DESeq2. *Genome Biol* **15**, 1–21 (2014).
89. M. D. Robinson, D. J. McCarthy, G. K. Smyth, edgeR: A Bioconductor package for differential expression analysis of digital gene expression data. *Bioinformatics* **26**, 139–140 (2009).
90. J. R. Conway, A. Lex, N. Gehlenborg, UpSetR: An R package for the visualization of intersecting sets and their properties. *Bioinformatics* **33**, 2938–2940 (2017).
91. Z. Gu, L. Gu, R. Eils, M. Schlesner, B. Brors, Circlize implements and enhances circular visualization in R. *Bioinformatics* **30**, 2811–2812 (2014).

92. M. E. Ritchie, B. Phipson, D. Wu, Y. Hu, C. W. Law, W. Shi, G. K. Smyth, Limma powers differential expression analyses for RNA-sequencing and microarray studies. *Nucleic Acids Res* **43**, e47 (2015).

Acknowledgments: We thank L. Ortet, and M. Raya for their technical contributions, and members of the PMC lab for helpful discussions. We are also indebted to V.A. Raker for excellent manuscript editing, and D. Sebastian (IRB Barcelona) for help in metabolic cages analysis, A. Dopazo (CNIC-Genomics Facility) for help in transcriptomics, J.A. Fernández-Blanco (PRBB Animal Facility) for animal care, and X. Sanjuan for microscopy (PRBB ALMF). **Funding:** The authors acknowledge funding from MICINN-Spain (RTI2018-096068 to P.M.C. and E.P), ERC-2016-AdG-741966 to P.M.C, María-de-Maeztu Program for Units of Excellence to UPF (MDM-2014-0370), and Altos Labs Inc. Research in the S.A.B. lab is supported by ERC-787041, the Foundation Lilliane Bettencourt, the Spanish Association for Cancer Research (AECC), and The Worldwide Cancer Research Foundation (WCRF). The IRB Barcelona is a Severo Ochoa Center of Excellence (SEV-2015-0505). K.B.K. acknowledges funding from NIH F32 Fellowship - DK121425. P.P. was funded by The Wenner-Gren Foundations and The Foundation Blanceflor Boncompagni Ludovisi, née Bildt. C.M.G. acknowledges funding from European Union's Horizon 2020 Research and Innovation Programme under the Marie Sklodowska-Curie grant agreement 749869. P.P. was funded by The Wenner-Gren Foundations and The Foundation Blanceflor Boncompagni Ludovisi, née Bildt. V.M.Z. received financial support through the "la Caixa" INPhINIT Fellowship Grant for Doctoral Studies at Spanish Research Centers of Excellence, "la Caixa" Foundation, Barcelona (ID 100010434) with fellowship code (LCF/BQ/IN17/11620018). P.-S.W. is supported by grant RYC2019-026661-I funded by MCIN/AEI/10.13039/501100011033 and by "ESF Investing in your future". **Author contributions:** A.K. and P.M.C. conceptualized the work, designed the study, and supervised the overall experiments. M.V.D. and A.K. performed the majority of experiments. A.K. and O.D. performed the bioinformatics data analysis of the circadian transcriptomes. J.S., V.L., and E.A. provided technical experimental assistance in mice sample collection, immunohistochemistry, and in vivo transfections. A.K. and M.V.D. interpreted the experimental data. A.K and M.V.D wrote the manuscript with P.M.C. and critical input from all other authors. T.M., JG.S., P.P., K.B.K., C.M.G., and V.M.Z., helped with manuscript editing. A.S., E.P. helped in the manuscript organization, data analysis, and interpretation of the results. P.S.W. and S.A.B. provided the Bmal1-StopFL mice strain used in this study. **Competing interest:** A.L.S., E.P., and P.M.C. are investigators of Altos Labs. S.A.B. is a co-founder and scientific advisor of ONA Therapeutics. The other authors declare no competing interests. **Data and materials availability:** All data are available in the main text, supplementary materials,

or online storage. Supplementary tables are available on Dryad https://doi.org/10.5061/dryad.8931zcrxp . Raw and processed RNA-seq data are available at the NCBI's Gene Expression Omnibus database under the accessions GSE195724 and GSE225851. The code used to generate results central to the main conclusions is available upon request.

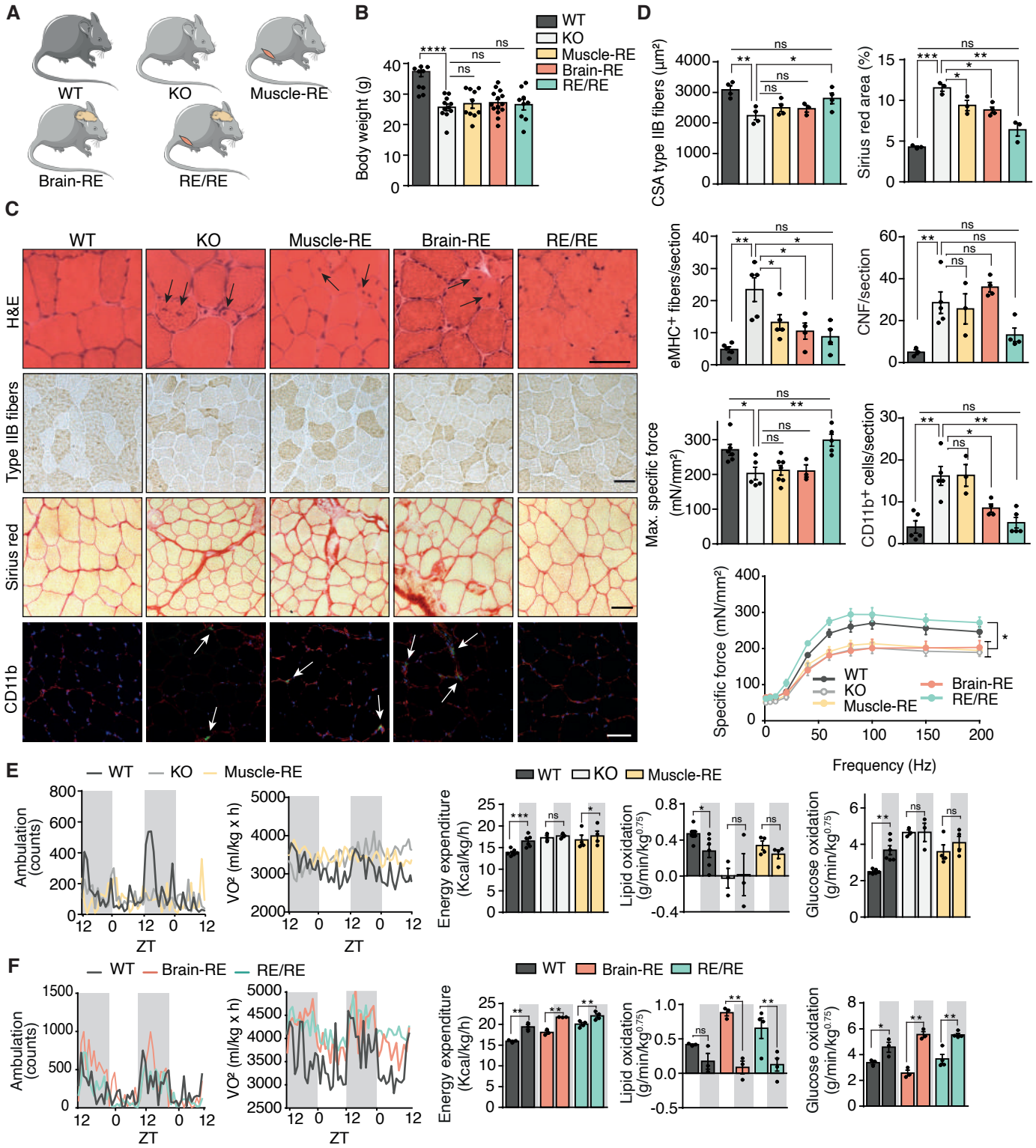
A
WT
KO
Muscle-RE
Brain-RE
RE/RE
B
Body weight (g)
WT
KO
Muscle-RE
Brain-RE
RE/RE
D
CSA type IIB fibers (µm²)
Sirius red area (%)
C
H&E
Type IIB fibers
Sirius red
CD11b
eMHC⁺ fibers/section
CNF/section
Max. specific force (mN/mm²)
CD11b⁺ cells/section
Specific force (mN/mm²)
Frequency (Hz)
E
Ambulation (counts)
VO² (ml/kg x h)
Energy expenditure (Kcal/kg/h)
Lipid oxidation (g/min/kg^0.75)
Glucose oxidation (g/min/kg^0.75)
ZT
F

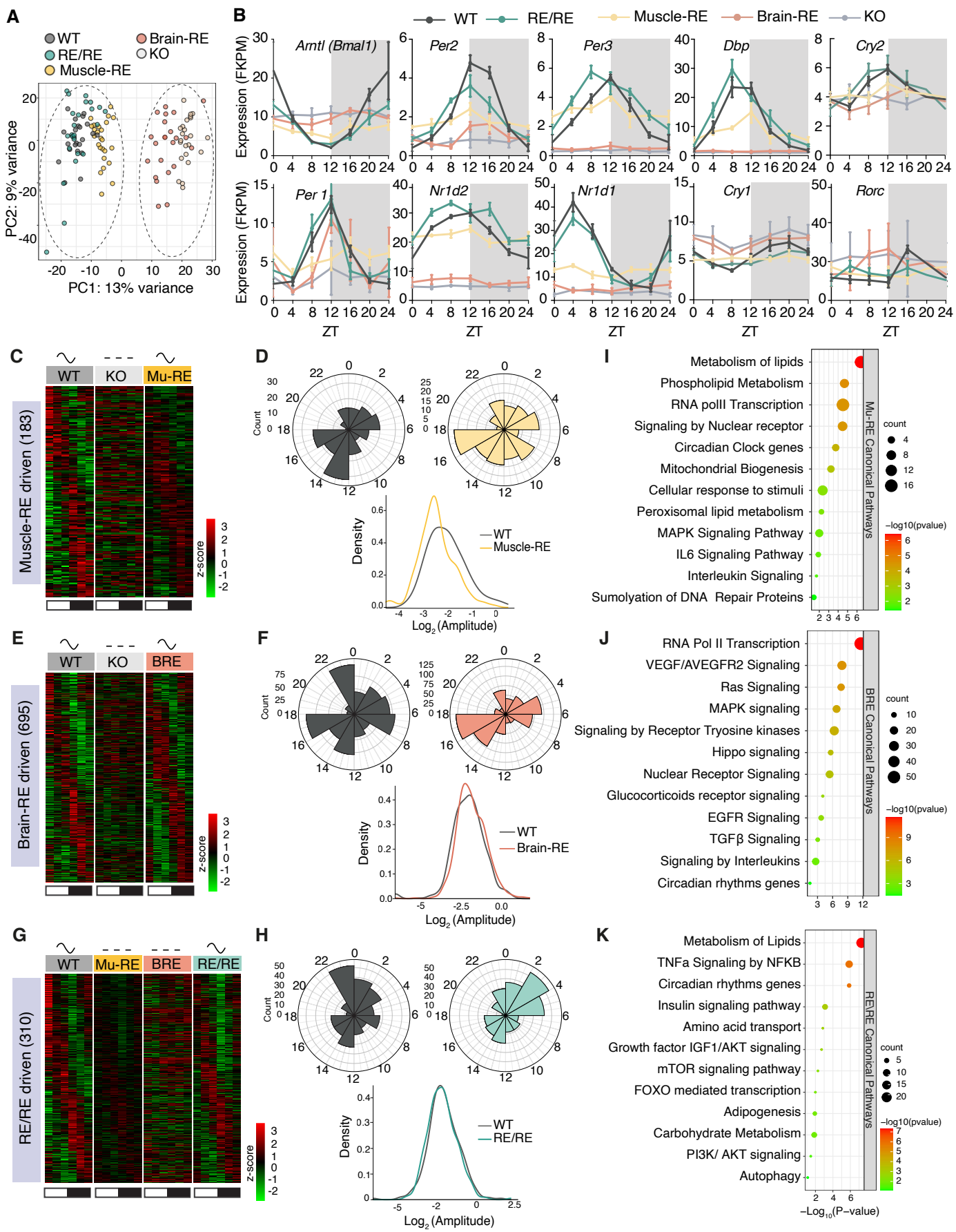
A
WT
RE/RE
Muscle-RE
Brain-RE
KO
PC2: 9% variance
PC1: 13% variance
B
WT
RE/RE
Muscle-RE
Brain-RE
KO
Arntl (Bmal1)
Per2
Per3
Dbp
Cry2
Per 1
Nr1d2
Nr1d1
Cry1
Rorc
Expression (FKPM)
ZT
C
WT
KO
Mu-RE
Muscle-RE driven (183)
z-score
D
Count
Density
WT
Muscle-RE
Log2 (Amplitude)
I
Metabolism of lipids
Phospholipid Metabolism
RNA polII Transcription
Signaling by Nuclear receptor
Circadian Clock genes
Mitochondrial Biogenesis
Cellular response to stimuli
Peroxisomal lipid metabolism
MAPK Signaling Pathway
IL6 Signaling Pathway
Interleukin Signaling
Sumolyation of DNA Repair Proteins
Mu-RE Canonical Pathways
count
–log10(pvalue)
E
WT
KO
BRE
Brain-RE driven (695)
z-score
F
Count
Density
WT
Brain-RE
Log2 (Amplitude)
J
RNA Pol II Transcription
VEGF/AVEGFR2 Signaling
Ras Signaling
MAPK signaling
Signaling by Receptor Tyrosine kinases
Hippo signaling
Nuclear Receptor Signaling
Glucocorticoids receptor signaling
EGFR Signaling
TGFβ Signaling
Signaling by Interleukins
Circadian rhythms genes
BRE Canonical Pathways
count
–log10(pvalue)
G
WT
Mu-RE
BRE
RE/RE
RE/RE driven (310)
z-score
H
Count
Density
WT
RE/RE
Log2 (Amplitude)
K
Metabolism of Lipids
TNFa Signaling by NFKB
Circadian rhythms genes
Insulin signaling pathway
Amino acid transport
Growth factor IGF1/AKT signaling
mTOR signaling pathway
FOXO mediated transcription
Adipogenesis
Carbohydrate Metabolism
PI3K/ AKT signaling
Autophagy
RERE Canonical Pathways
count
–log10(pvalue)
–Log10(P–value)

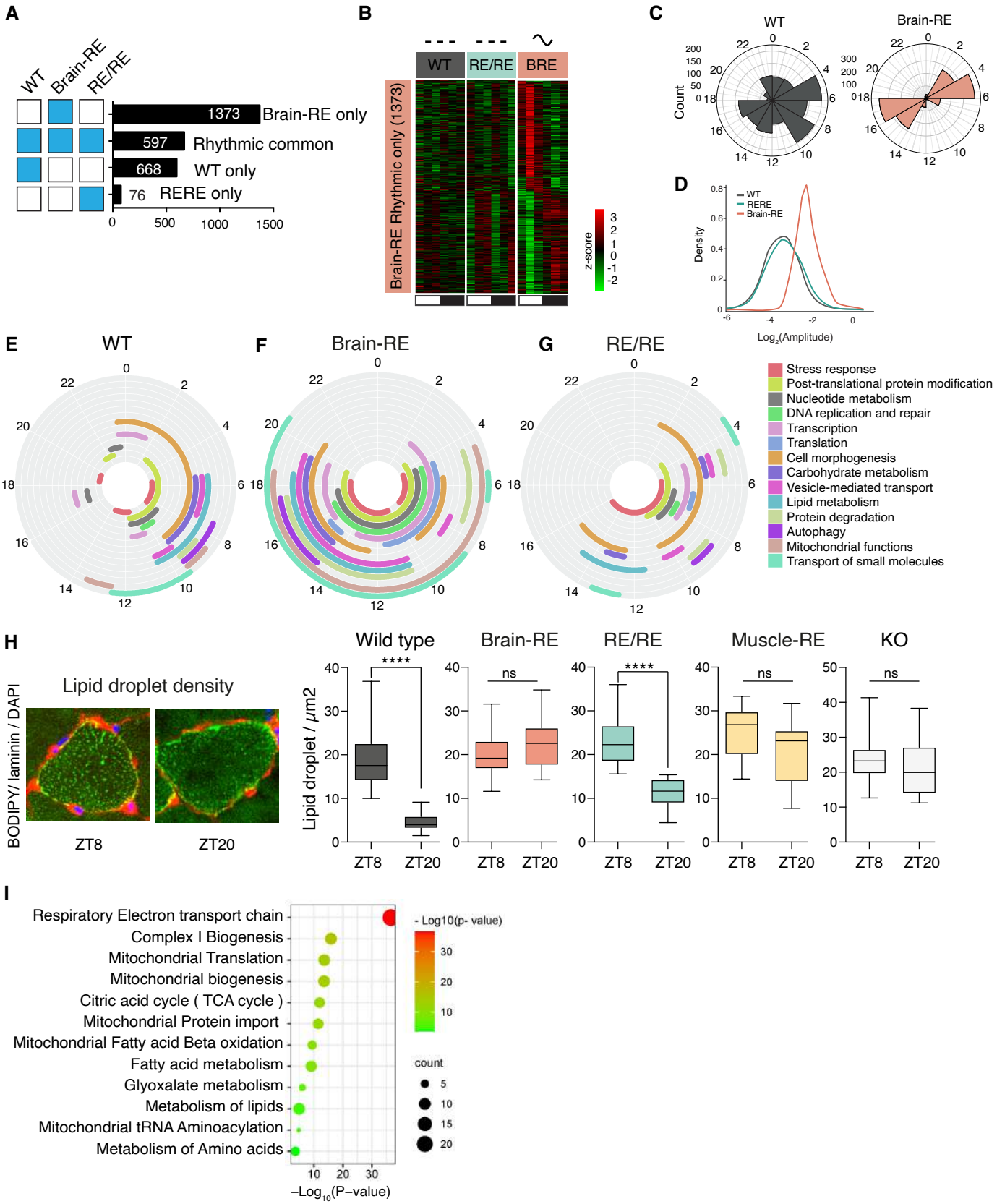
A
WT
Brain-RE
RE/RE
1373
Brain-RE only
597
Rhythmic common
668
WT only
76
RERE only
0
500
1000
1500
B
WT
RE/RE
BRE
Brain-RE Rhythmic only (1373)
z-score
3
2
1
0
-1
-2
C
WT
Brain-RE
Count
D
WT
RERE
Brain-RE
Density
Log2(Amplitude)
E
WT
F
Brain-RE
G
RE/RE
Stress response
Post-translational protein modification
Nucleotide metabolism
DNA replication and repair
Transcription
Translation
Cell morphogenesis
Carbohydrate metabolism
Vesicle-mediated transport
Lipid metabolism
Protein degradation
Autophagy
Mitochondrial functions
Transport of small molecules
H
Lipid droplet density
BODIPY/ laminin / DAPI
ZT8
ZT20
Wild type
Brain-RE
RE/RE
Muscle-RE
KO
Lipid droplet / μm2
****
ns
I
Respiratory Electron transport chain
Complex I Biogenesis
Mitochondrial Translation
Mitochondrial biogenesis
Citric acid cycle (TCA cycle)
Mitochondrial Protein import
Mitochondrial Fatty acid Beta oxidation
Fatty acid metabolism
Glyoxalate metabolism
Metabolism of lipids
Mitochondrial tRNA Aminoacylation
Metabolism of Amino acids
- Log10(p- value)
count
–Log10(P–value)

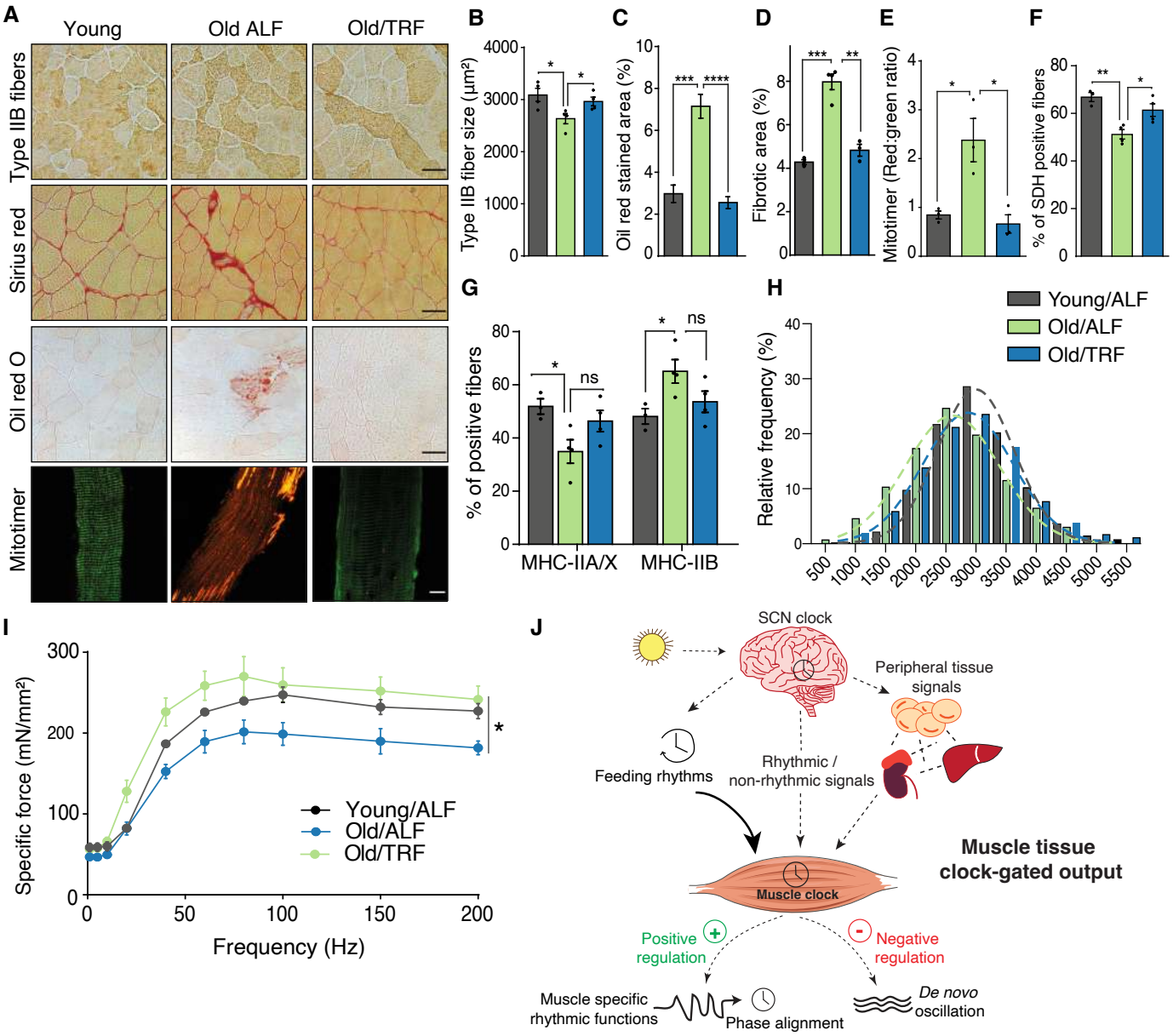
A
Young
Old ALF
Old/TRF
Type IIB fibers
Sirius red
Oil red O
Mitotimer
B
Type IIB fiber size (µm²)
C
Oil red stained area (%)
D
Fibrotic area (%)
E
Mitotimer (Red:green ratio)
F
% of SDH positive fibers
G
% of positive fibers
MHC-IIA/X
MHC-IIB
ns
H
Relative frequency (%)
Young/ALF
Old/ALF
Old/TRF
I
Specific force (mN/mm²)
Frequency (Hz)
Young/ALF
Old/ALF
Old/TRF
J
SCN clock
Peripheral tissue signals
Feeding rhythms
Rhythmic / non-rhythmic signals
Muscle clock
Muscle tissue clock-gated output
Positive regulation
Negative regulation
Muscle specific rhythmic functions
Phase alignment
De novo oscillation

Figure S1

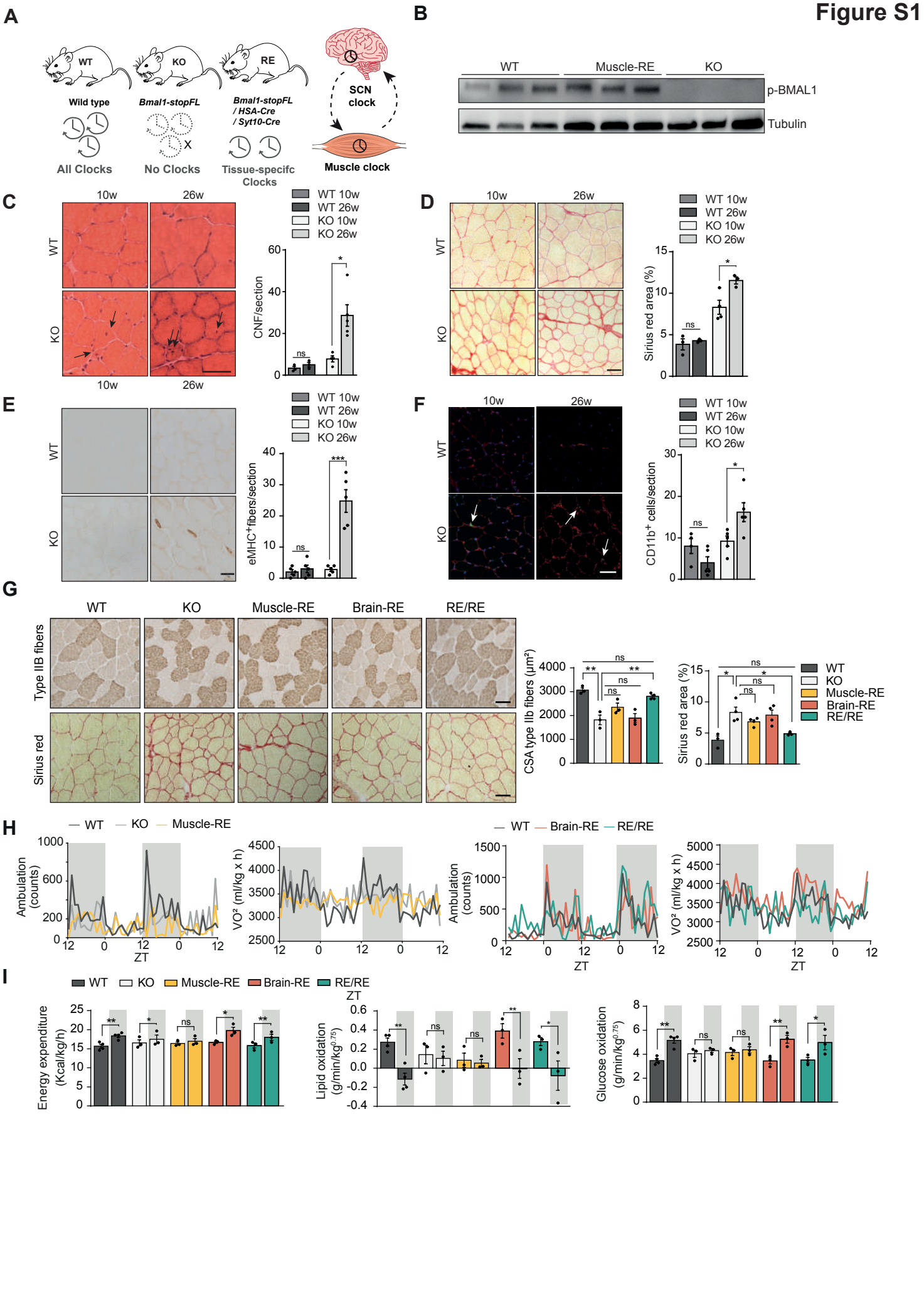
A
WT
KO
RE
Wild type
Bmal1-stopFL
Bmal1-stopFL / HSA-Cre / Syt10-Cre
All Clocks
No Clocks
Tissue-specifc Clocks
SCN clock
Muscle clock
B
WT
Muscle-RE
KO
p-BMAL1
Tubulin
C
10w
26w
WT
KO
WT 10w
WT 26w
KO 10w
KO 26w
CNF/section
ns
D
Sirius red area (%)
E
eMHC+fibers/section
F
CD11b+ cells/section
G
WT
KO
Muscle-RE
Brain-RE
RE/RE
Type IIB fibers
Sirius red
CSA type IIb fibers (µm²)
Sirius red area (%)
H
Ambulation (counts)
VO² (ml/kg x h)
ZT
I
Energy expenditure (Kcal/kg/h)
Lipid oxidation (g/min/kg^0.75)
Glucose oxidation (g/min/kg^0.75)

Figure S2

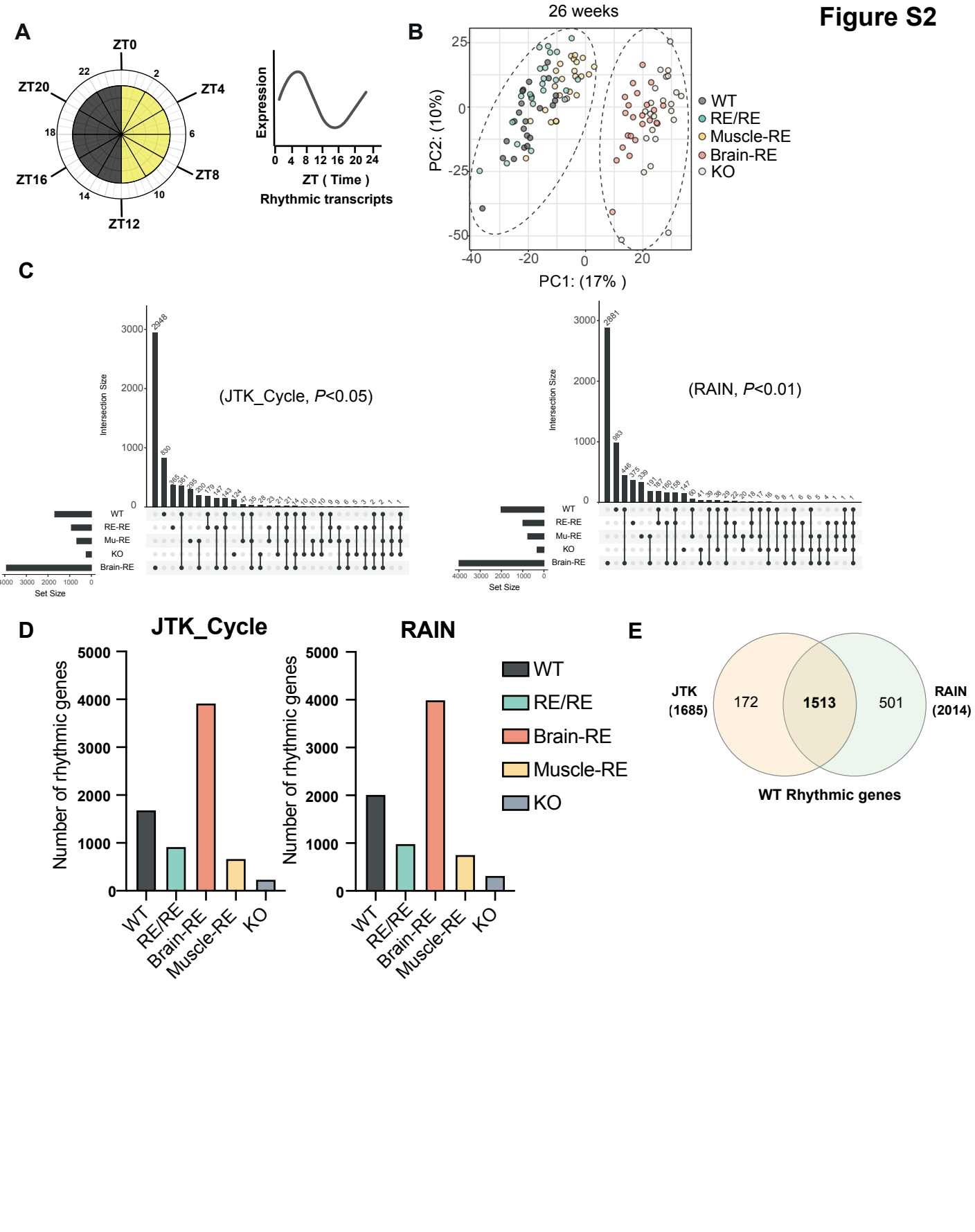
A
ZT0
ZT4
ZT8
ZT12
ZT16
ZT20
Expression
ZT (Time)
Rhythmic transcripts
B
26 weeks
PC2: (10%)
PC1: (17%)
WT
RE/RE
Muscle-RE
Brain-RE
KO
C
(JTK_Cycle, P<0.05)
(RAIN, P<0.01)
Intersection Size
Set Size
WT
RE-RE
Mu-RE
KO
Brain-RE
D
JTK_Cycle
RAIN
Number of rhythmic genes
E
JTK
(1685)
172
1513
501
RAIN
(2014)
WT Rhythmic genes

Figure S3

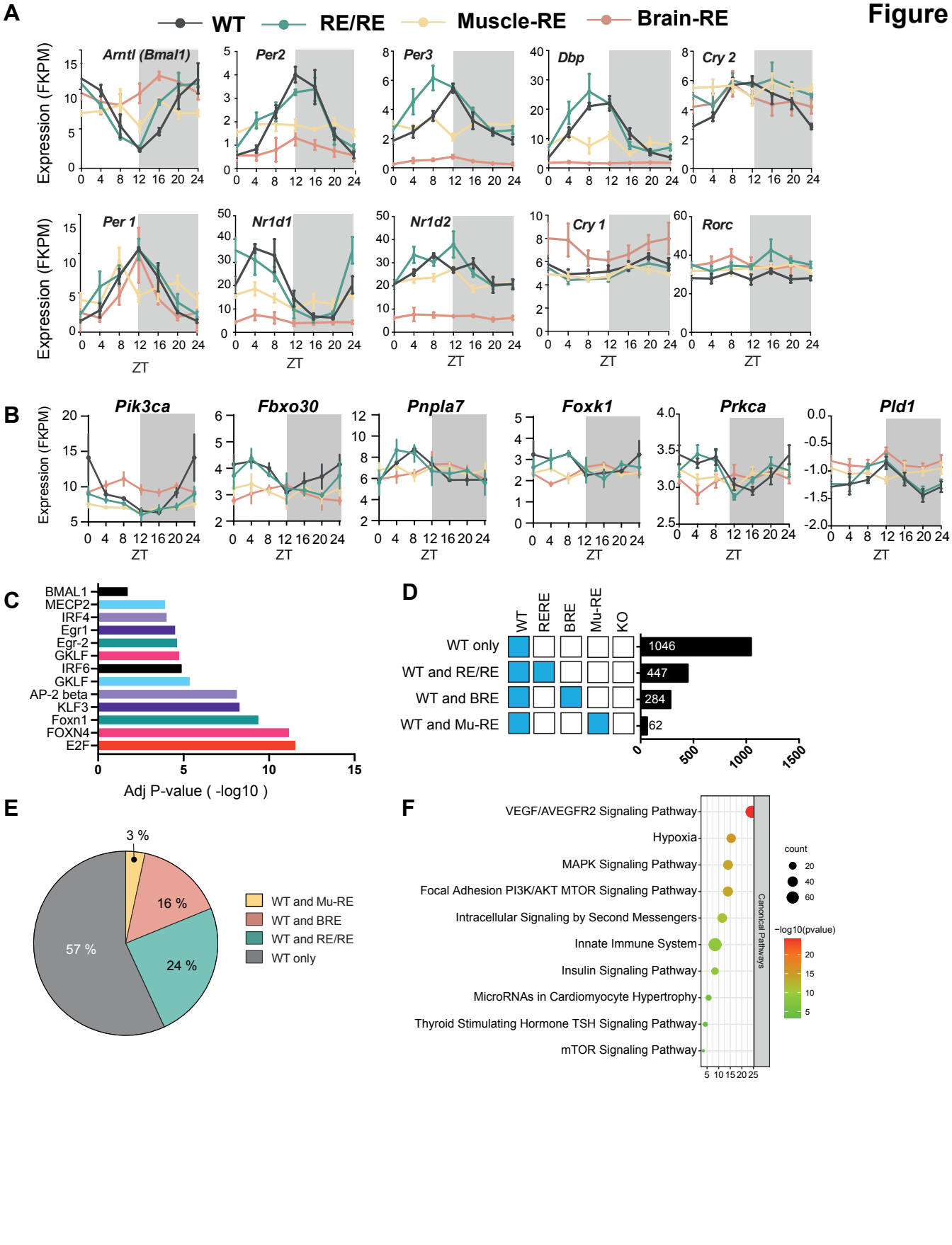
A
WT
RE/RE
Muscle-RE
Brain-RE
Arntl (Bmal1)
Per2
Per3
Dbp
Cry 2
Per 1
Nr1d1
Nr1d2
Cry 1
Rorc
Expression (FKPM)
ZT
B
Pik3ca
Fbxo30
Pnpla7
Foxk1
Prkca
Pld1
C
BMAL1
MECP2
IRF4
Egr1
Egr-2
GKLF
IRF6
GKLF
AP-2 beta
KLF3
Foxn1
FOXN4
E2F
Adj P-value (-log10)
D
WT
RERE
BRE
Mu-RE
KO
WT only
WT and RE/RE
WT and BRE
WT and Mu-RE
1046
447
284
62
E
3 %
16 %
24 %
57 %
WT and Mu-RE
WT and BRE
WT and RE/RE
WT only
F
VEGF/AVEGFR2 Signaling Pathway
Hypoxia
MAPK Signaling Pathway
Focal Adhesion PI3K/AKT MTOR Signaling Pathway
Intracellular Signaling by Second Messengers
Innate Immune System
Insulin Signaling Pathway
MicroRNAs in Cardiomyocyte Hypertrophy
Thyroid Stimulating Hormone TSH Signaling Pathway
mTOR Signaling Pathway
Canonical Pathways
count
−log10(pvalue)

Figure S4

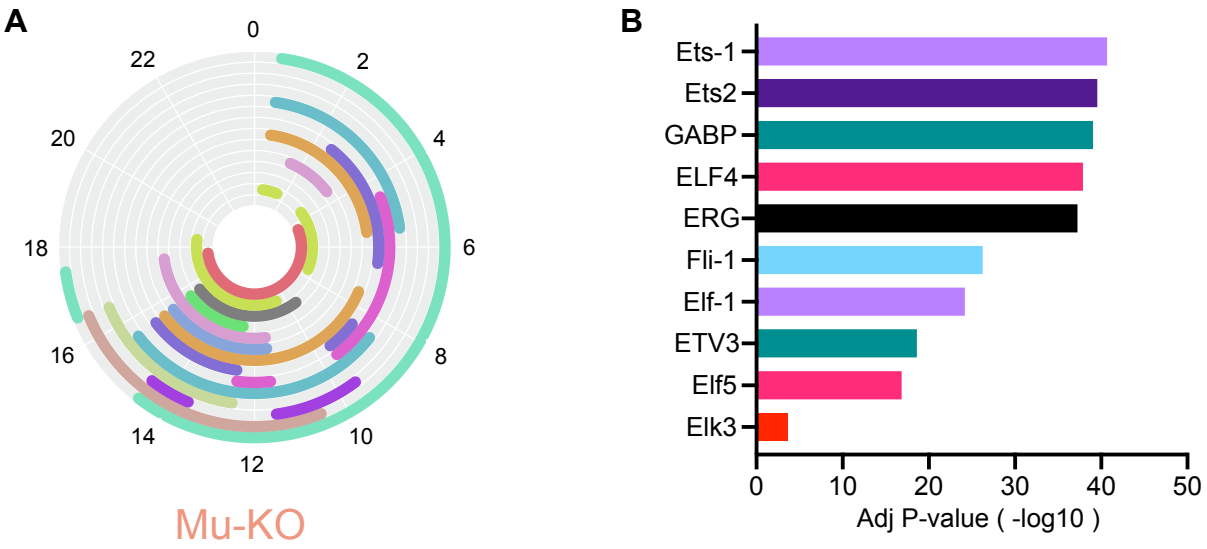
A
0
2
4
6
8
10
12
14
16
18
20
22
Mu-KO
B
Ets-1
Ets2
GABP
ELF4
ERG
Fli-1
Elf-1
ETV3
Elf5
Elk3
0
10
20
30
40
50
Adj P-value (-log10)

Figure S5

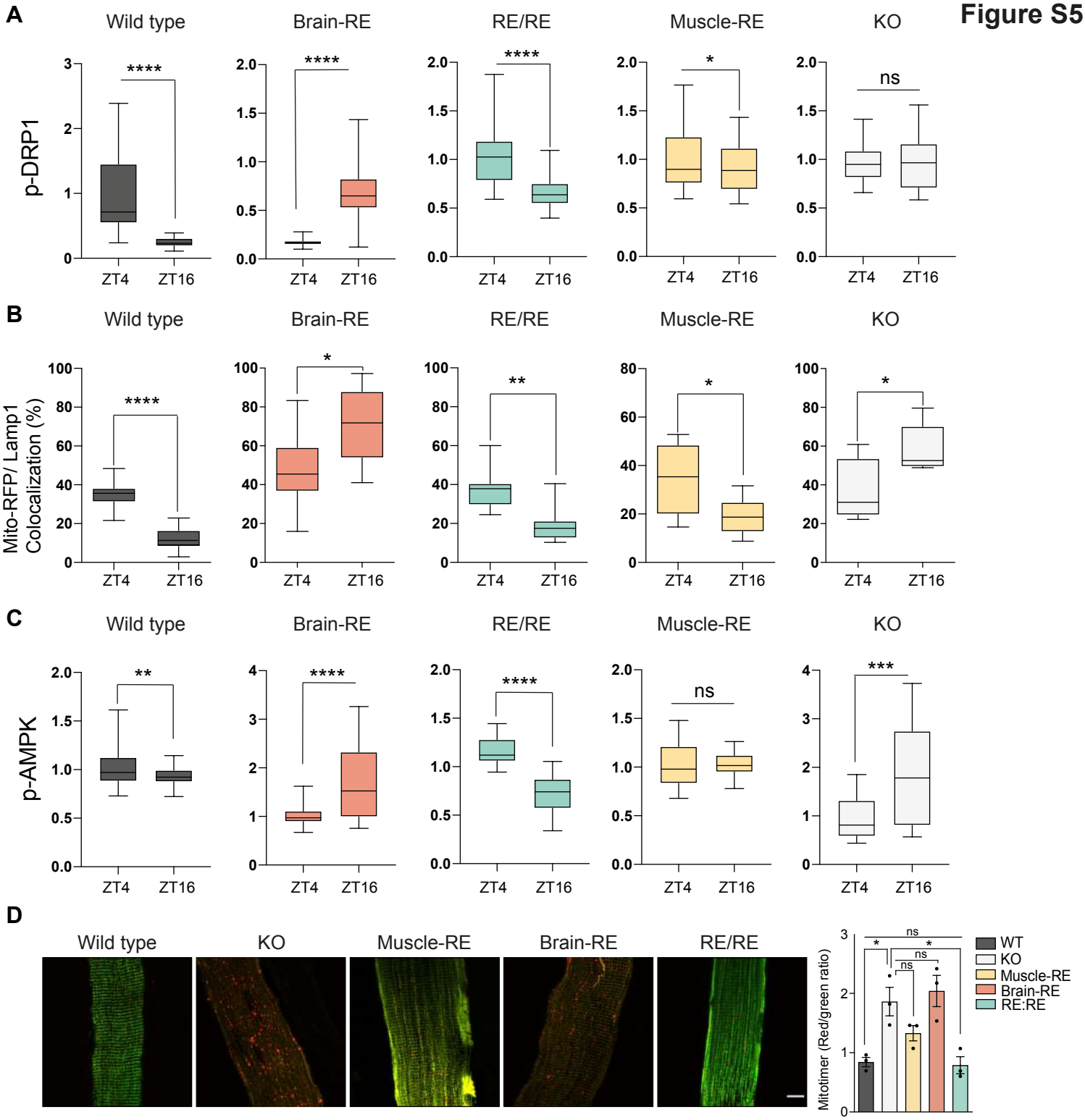
A
Wild type
Brain-RE
RE/RE
Muscle-RE
KO
p-DRP1
****
****
****
*
ns
ZT4
ZT16
B
Wild type
Brain-RE
RE/RE
Muscle-RE
KO
Mito-RFP/ Lamp1 Colocalization (%)
****
*
**
*
*
C
Wild type
Brain-RE
RE/RE
Muscle-RE
KO
p-AMPK
**
****
****
ns
***
D
Wild type
KO
Muscle-RE
Brain-RE
RE/RE
Mitotimer (Red/green ratio)
WT
KO
Muscle-RE
Brain-RE
RE:RE

Figure S6

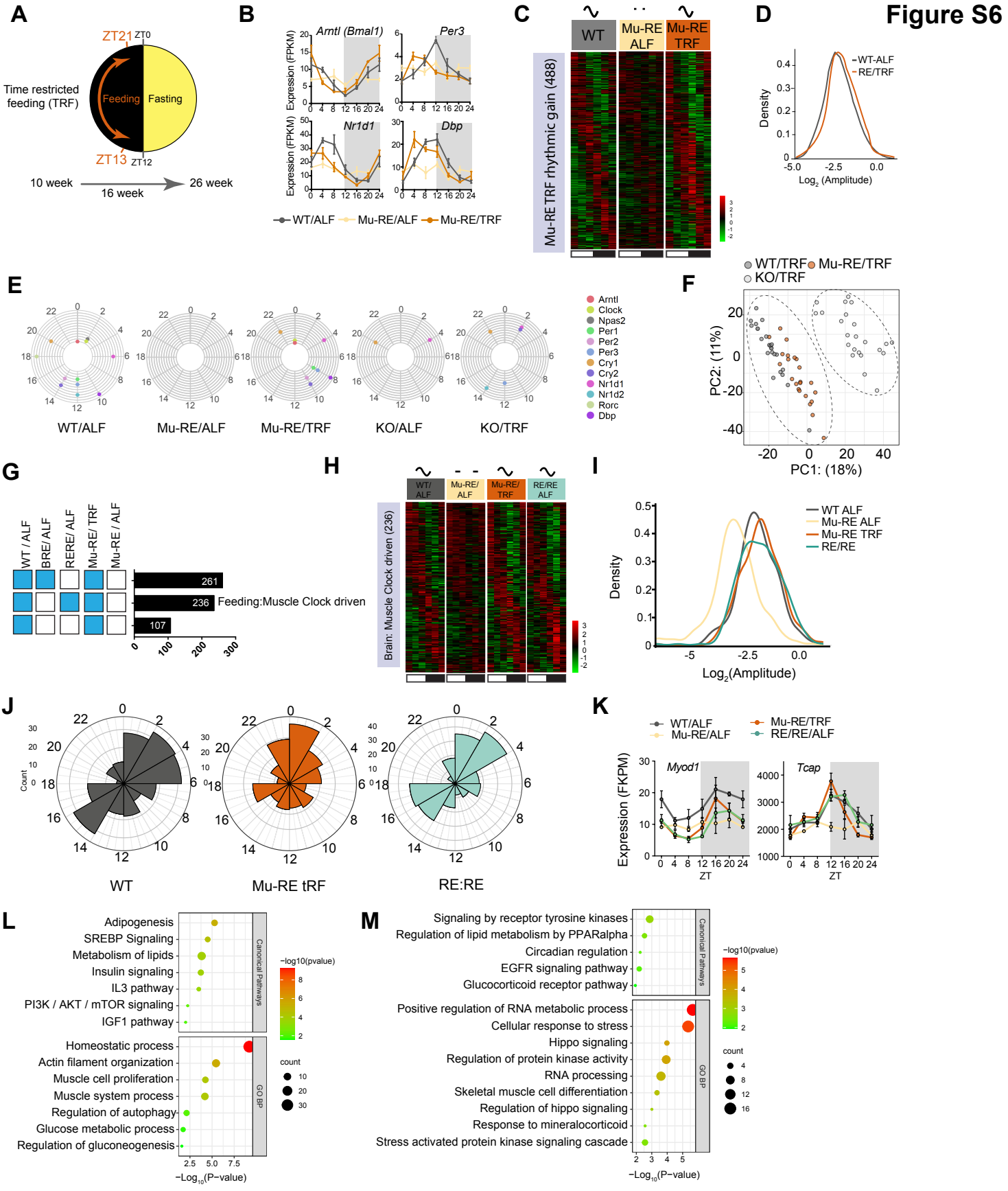
A
ZT21
ZT0
Time restricted feeding (TRF)
Feeding
Fasting
ZT13
ZT12
10 week
16 week
26 week
B
Arntl (Bmal1)
Per3
Nr1d1
Dbp
Expression (FPKM)
WT/ALF
Mu-RE/ALF
Mu-RE/TRF
C
WT
Mu-RE ALF
Mu-RE TRF
Mu-RE TRF rhythmic gain (488)
D
WT-ALF
RE/TRF
Density
Log2 (Amplitude)
E
Arntl
Clock
Npas2
Per1
Per2
Per3
Cry1
Cry2
Nr1d1
Nr1d2
Rorc
Dbp
WT/ALF
Mu-RE/ALF
Mu-RE/TRF
KO/ALF
KO/TRF
F
WT/TRF
Mu-RE/TRF
KO/TRF
PC2: (11%)
PC1: (18%)
G
WT / ALF
BRE/ ALF
RERE/ ALF
Mu-RE/ TRF
Mu-RE / ALF
261
236
107
Feeding:Muscle Clock driven
H
WT/ ALF
Mu-RE/ ALF
Mu-RE/ TRF
RE/RE ALF
Brain: Muscle Clock driven (236)
I
WT ALF
Mu-RE ALF
Mu-RE TRF
RE/RE
Density
Log2(Amplitude)
J
Count
WT
Mu-RE tRF
RE:RE
K
WT/ALF
Mu-RE/ALF
Mu-RE/TRF
RE/RE/ALF
Myod1
Tcap
Expression (FKPM)
ZT
L
Adipogenesis
SREBP Signaling
Metabolism of lipids
Insulin signaling
IL3 pathway
PI3K / AKT / mTOR signaling
IGF1 pathway
Homeostatic process
Actin filament organization
Muscle cell proliferation
Muscle system process
Regulation of autophagy
Glucose metabolic process
Regulation of gluconeogenesis
Canonical Pathways
GO BP
−log10(pvalue)
count
−Log10(P−value)
M
Signaling by receptor tyrosine kinases
Regulation of lipid metabolism by PPARalpha
Circadian regulation
EGFR signaling pathway
Glucocorticoid receptor pathway
Positive regulation of RNA metabolic process
Cellular response to stress
Hippo signaling
Regulation of protein kinase activity
RNA processing
Skeletal muscle cell differentiation
Regulation of hippo signaling
Response to mineralocorticoid
Stress activated protein kinase signaling cascade
Canonical Pathways
GO BP
−log10(pvalue)
count
−Log10(P−value)

Figure S7

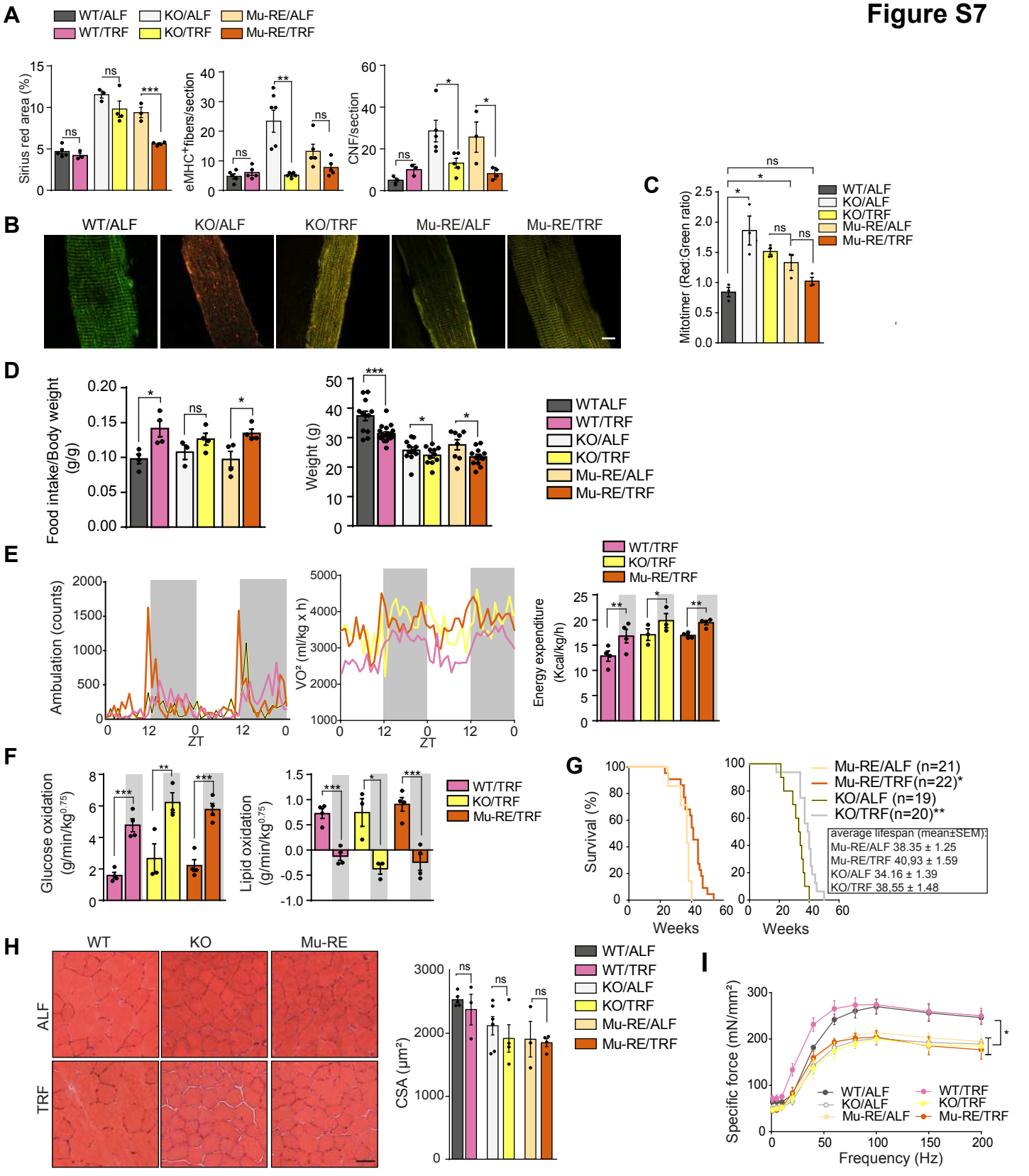
A
WT/ALF
WT/TRF
KO/ALF
KO/TRF
Mu-RE/ALF
Mu-RE/TRF
Sirius red area (%)
eMHC+fibers/section
CNF/section
B
WT/ALF
KO/ALF
KO/TRF
Mu-RE/ALF
Mu-RE/TRF
C
Mitotimer (Red:Green ratio)
D
Food intake/Body weight (g/g)
Weight (g)
WTALF
E
Ambulation (counts)
VO² (ml/kg x h)
Energy expenditure (Kcal/kg/h)
ZT
F
Glucose oxidation (g/min/kg^0.75)
Lipid oxidation (g/min/kg^0.75)
G
Survival (%)
Weeks
Mu-RE/ALF (n=21)
Mu-RE/TRF(n=22)*
KO/ALF (n=19)
KO/TRF(n=20)**
average lifespan (mean±SEM):
Mu-RE/ALF 38.35 ± 1.25
Mu-RE/TRF 40,93 ± 1.59
KO/ALF 34.16 ± 1.39
KO/TRF 38,55 ± 1.48
H
WT
KO
Mu-RE
ALF
TRF
CSA (µm²)
I
Specific force (mN/mm²)
Frequency (Hz)

Figure S8

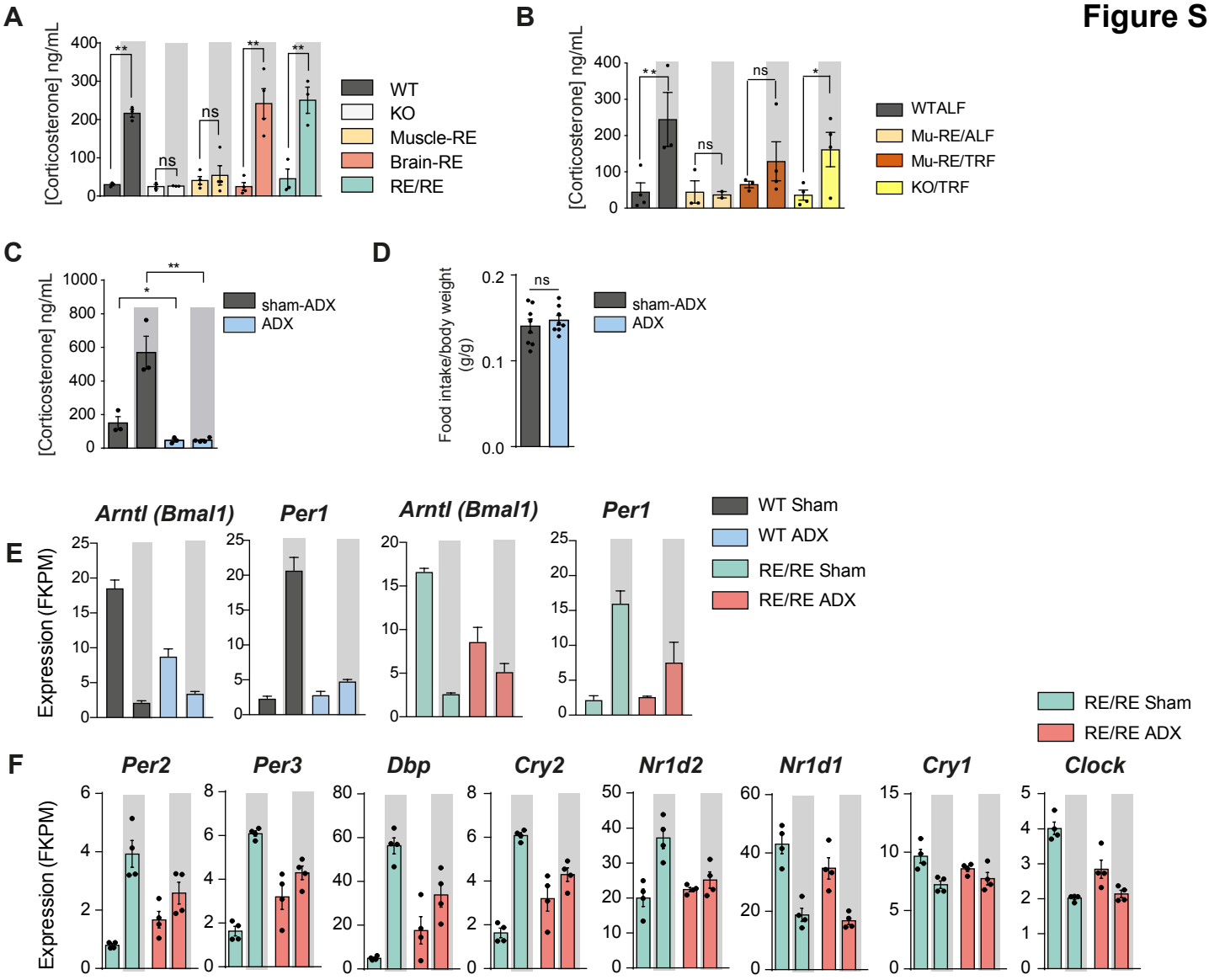
A
[Corticosterone] ng/mL
WT
KO
Muscle-RE
Brain-RE
RE/RE
B
[Corticosterone] ng/mL
WTALF
Mu-RE/ALF
Mu-RE/TRF
KO/TRF
C
[Corticosterone] ng/mL
sham-ADX
ADX
D
Food intake/body weight (g/g)
sham-ADX
ADX
E
Arntl (Bmal1)
Per1
Arntl (Bmal1)
Per1
Expression (FKPM)
WT Sham
WT ADX
RE/RE Sham
RE/RE ADX
F
Per2
Per3
Dbp
Cry2
Nr1d2
Nr1d1
Cry1
Clock
Expression (FKPM)
RE/RE Sham
RE/RE ADX

Figure S9

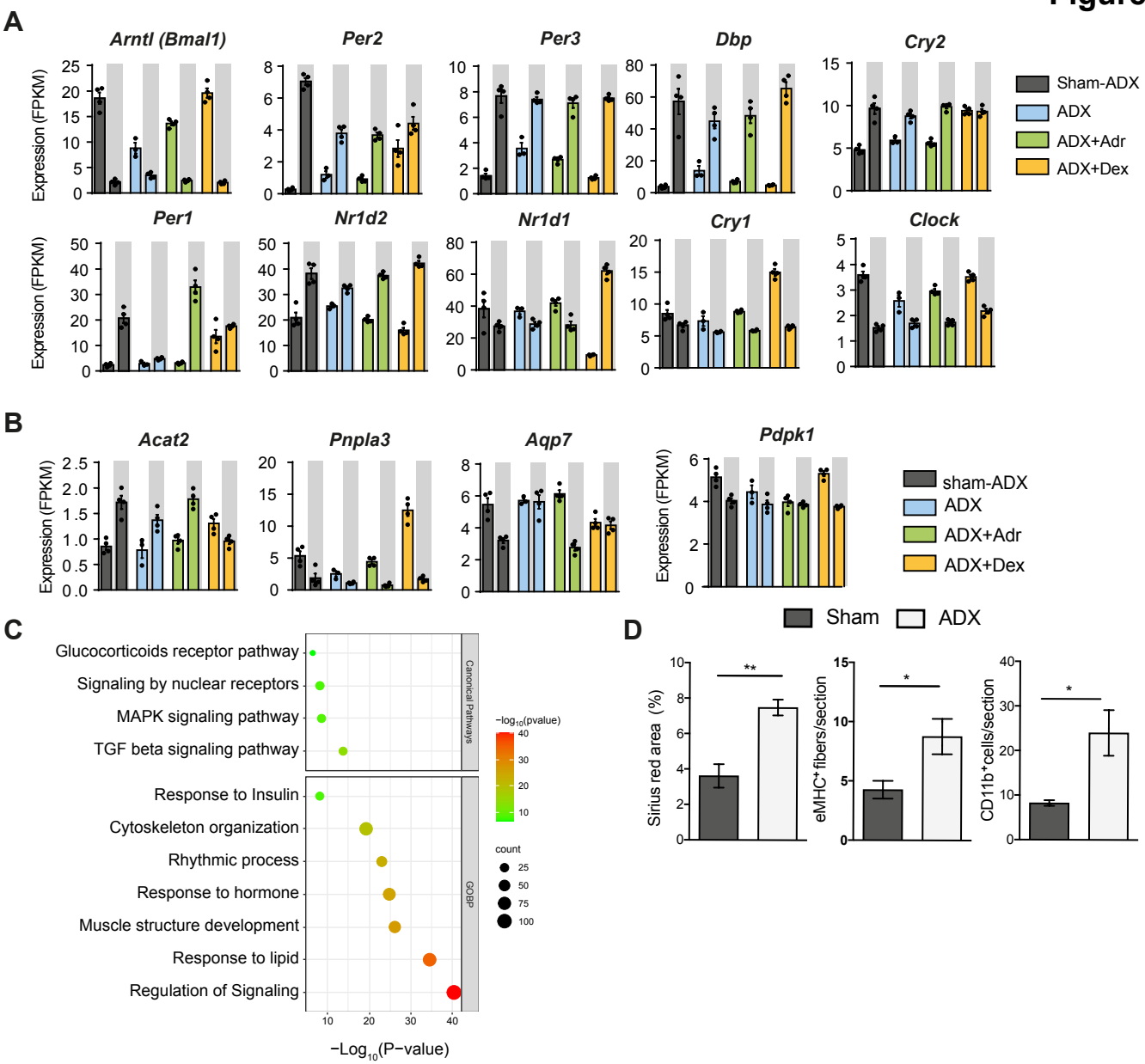
A
Arntl (Bmal1)
Per2
Per3
Dbp
Cry2
Per1
Nr1d2
Nr1d1
Cry1
Clock
Expression (FPKM)
Sham-ADX
ADX
ADX+Adr
ADX+Dex
B
Acat2
Pnpla3
Aqp7
Pdpk1
Expression (FPKM)
sham-ADX
ADX
ADX+Adr
ADX+Dex
C
Glucocorticoids receptor pathway
Signaling by nuclear receptors
MAPK signaling pathway
TGF beta signaling pathway
Response to Insulin
Cytoskeleton organization
Rhythmic process
Response to hormone
Muscle structure development
Response to lipid
Regulation of Signaling
Canonical Pathways
GOBP
−log10(pvalue)
count
−Log10(P−value)
D
Sham
ADX
Sirius red area (%)
eMHC+ fibers/section
CD11b+cells/section

Figure S10

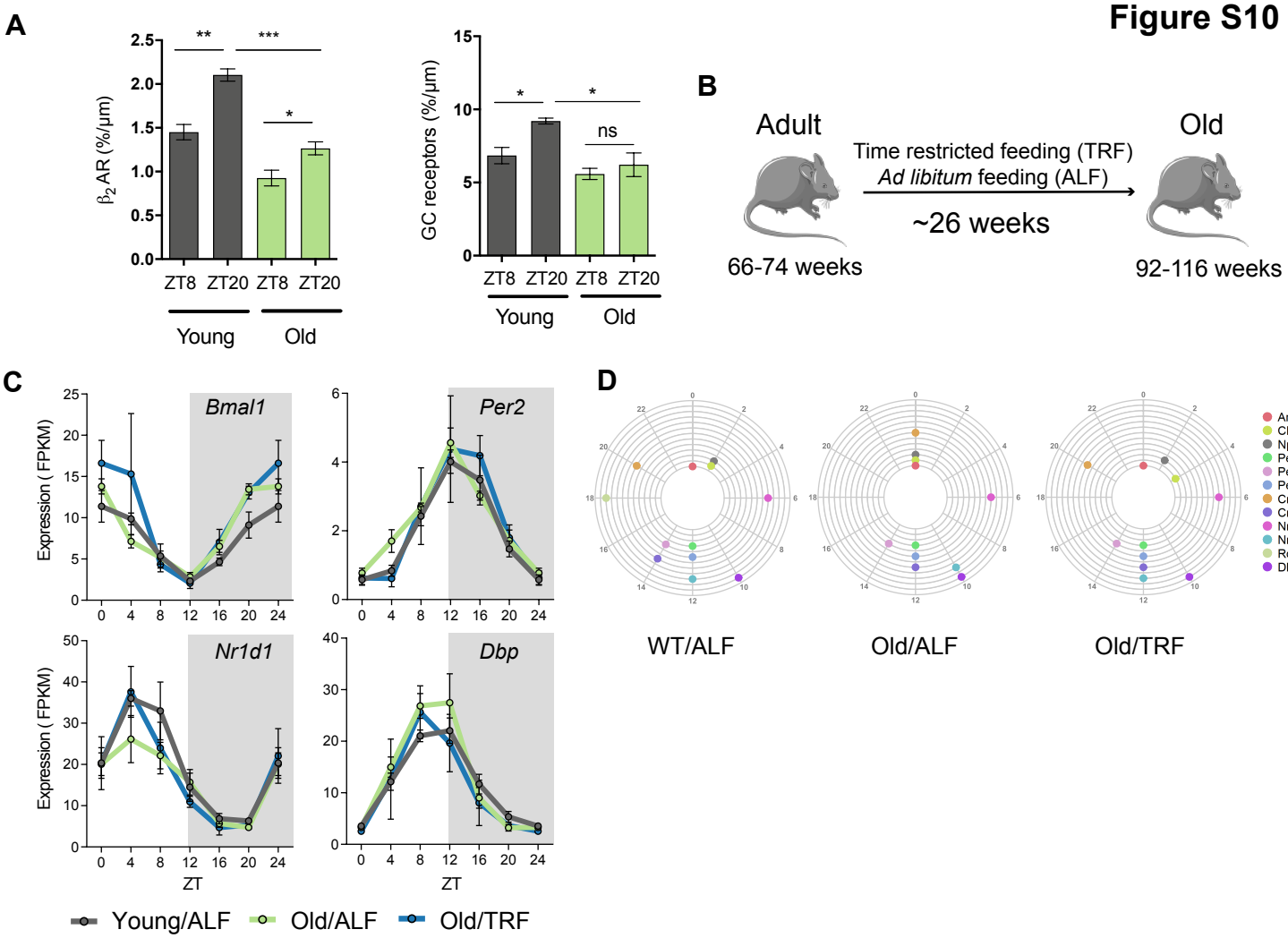
A
β_2AR (%/µm)
GC receptors (%/µm)
ZT8 ZT20 ZT8 ZT20
Young
Old
ns
B
Adult
Old
Time restricted feeding (TRF)
Ad libitum feeding (ALF)
~26 weeks
66-74 weeks
92-116 weeks
C
Bmal1
Per2
Nr1d1
Dbp
Expression (FPKM)
ZT
Young/ALF
Old/ALF
Old/TRF
D
WT/ALF
Old/ALF
Old/TRF
Arntl
Clock
Npas2
Per1
Per2
Per3
Cry1
Cry2
Nr1d1
Nr1d2
Rorc
Dbp

Figure S11

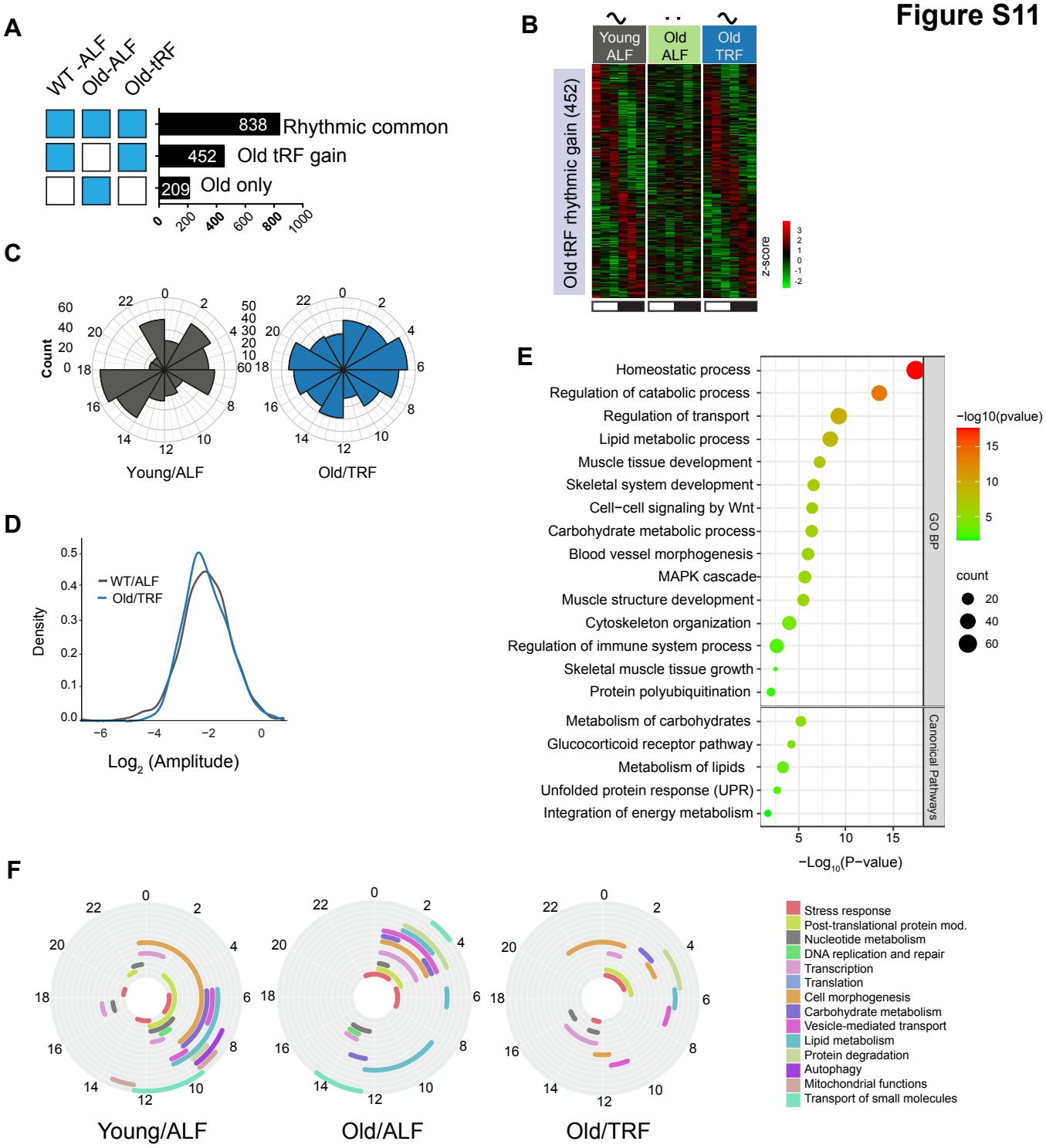
A
WT -ALF
Old-ALF
Old-tRF
838
Rhythmic common
452
Old tRF gain
209
Old only
0
200
400
600
800
1000
B
Young ALF
Old ALF
Old TRF
Old tRF rhythmic gain (452)
z-score
C
Count
Young/ALF
Old/TRF
D
WT/ALF
Old/TRF
Density
Log2 (Amplitude)
E
Homeostatic process
Regulation of catabolic process
Regulation of transport
Lipid metabolic process
Muscle tissue development
Skeletal system development
Cell−cell signaling by Wnt
Carbohydrate metabolic process
Blood vessel morphogenesis
MAPK cascade
Muscle structure development
Cytoskeleton organization
Regulation of immune system process
Skeletal muscle tissue growth
Protein polyubiquitination
Metabolism of carbohydrates
Glucocorticoid receptor pathway
Metabolism of lipids
Unfolded protein response (UPR)
Integration of energy metabolism
GO BP
Canonical Pathways
−log10(pvalue)
count
−Log10(P−value)
F
Young/ALF
Old/ALF
Old/TRF
Stress response
Post-translational protein mod.
Nucleotide metabolism
DNA replication and repair
Transcription
Translation
Cell morphogenesis
Carbohydrate metabolism
Vesicle-mediated transport
Lipid metabolism
Protein degradation
Autophagy
Mitochondrial functions
Transport of small molecules

Figure S12

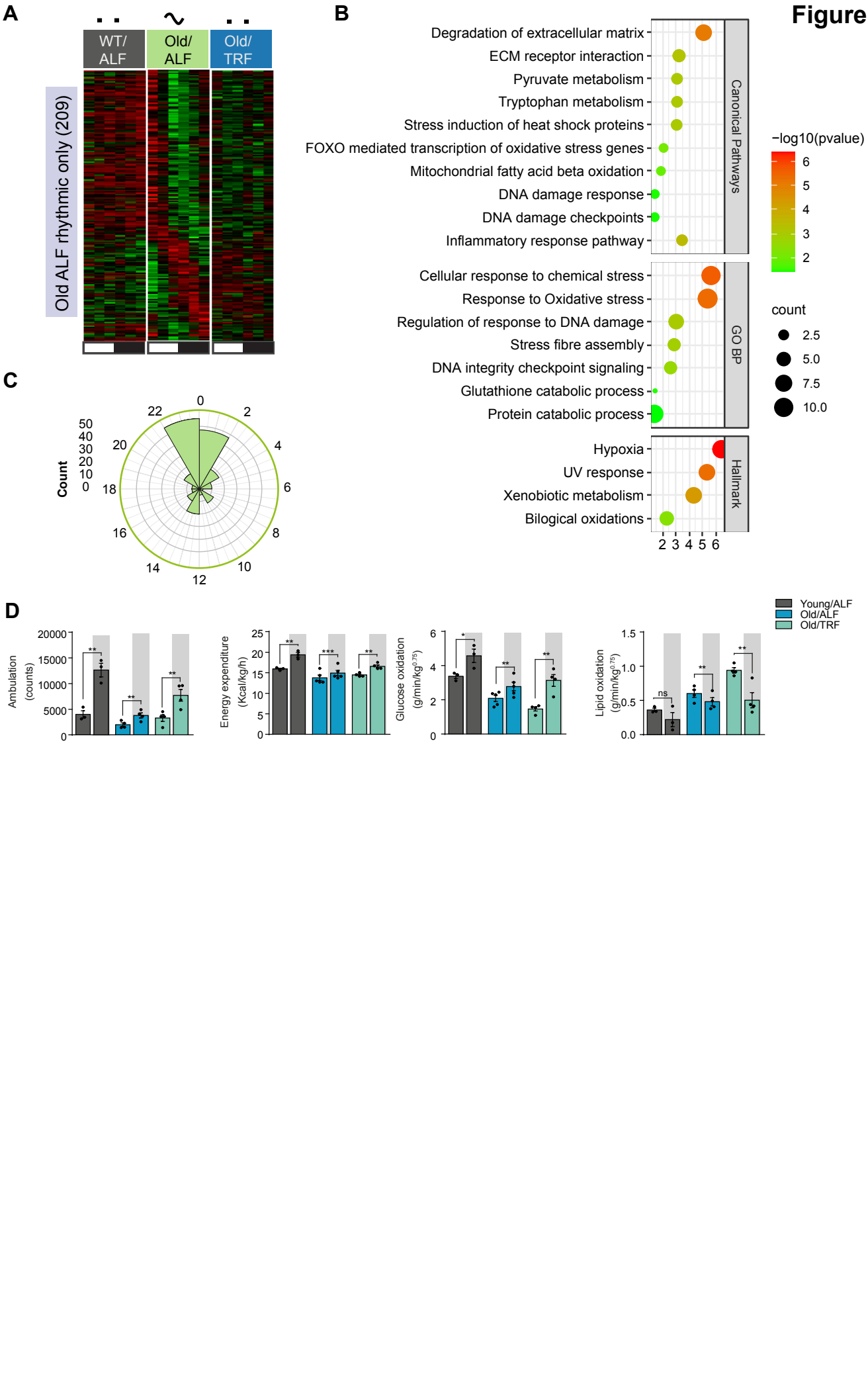
A
WT/ ALF
Old/ ALF
Old/ TRF
Old ALF rhythmic only (209)
B
Degradation of extracellular matrix
ECM receptor interaction
Pyruvate metabolism
Tryptophan metabolism
Stress induction of heat shock proteins
FOXO mediated transcription of oxidative stress genes
Mitochondrial fatty acid beta oxidation
DNA damage response
DNA damage checkpoints
Inflammatory response pathway
Canonical Pathways
Cellular response to chemical stress
Response to Oxidative stress
Regulation of response to DNA damage
Stress fibre assembly
DNA integrity checkpoint signaling
Glutathione catabolic process
Protein catabolic process
GO BP
Hypoxia
UV response
Xenobiotic metabolism
Bilogical oxidations
Hallmark
2 3 4 5 6
−log10(pvalue)
6
5
4
3
2
count
2.5
5.0
7.5
10.0
C
Count
50
40
30
20
10
0
0
2
4
6
8
10
12
14
16
18
20
22
D
Young/ALF
Old/ALF
Old/TRF
Ambulation (counts)
Energy expenditure (Kcal/kg/h)
Glucose oxidation (g/min/kg^0.75)
Lipid oxidation (g/min/kg^0.75)
ns

Figure S13

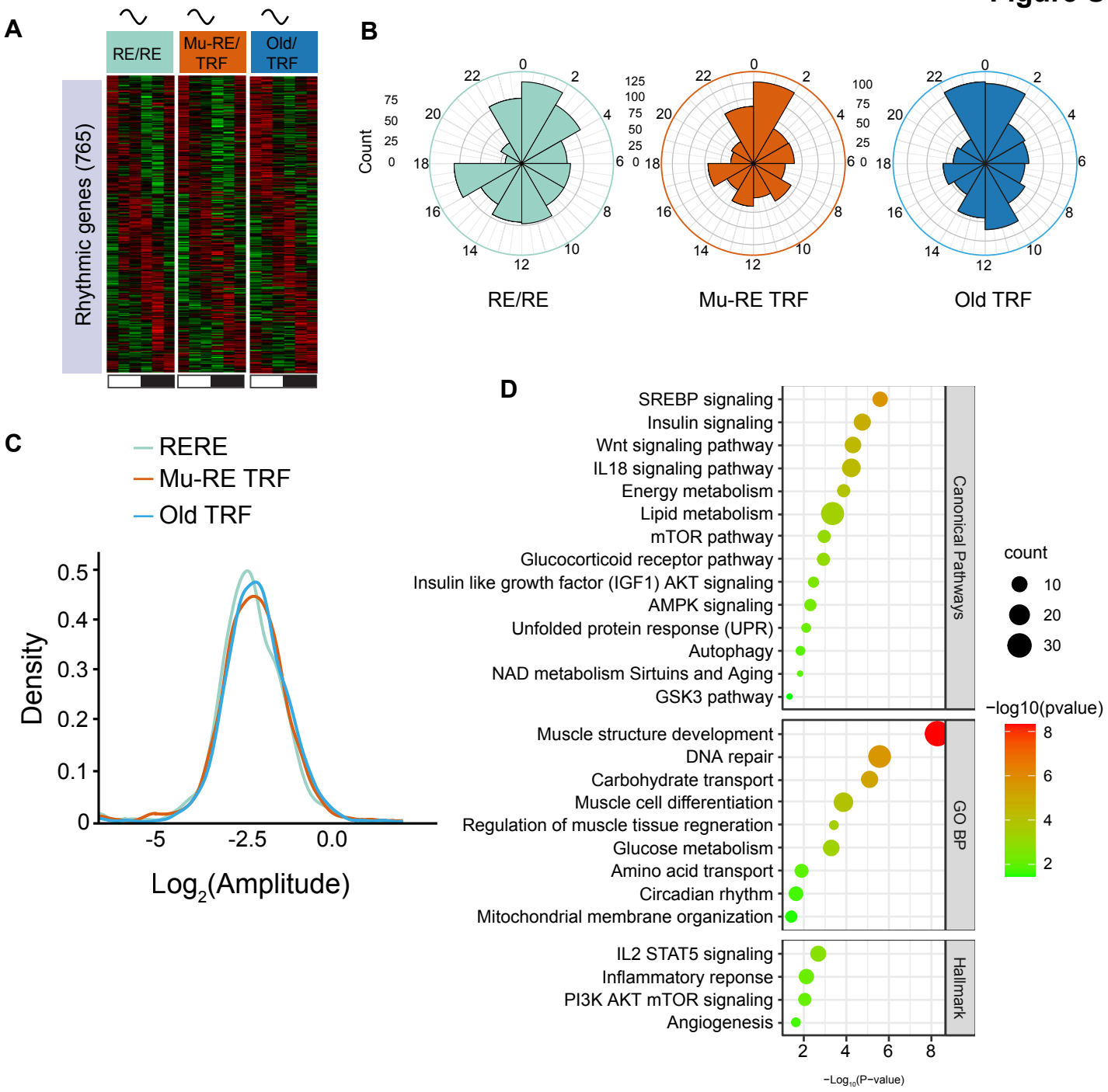
A
RE/RE
Mu-RE/ TRF
Old/ TRF
Rhythmic genes (765)
B
Count
RE/RE
Mu-RE TRF
Old TRF
C
RERE
Mu-RE TRF
Old TRF
Density
Log2(Amplitude)
D
SREBP signaling
Insulin signaling
Wnt signaling pathway
IL18 signaling pathway
Energy metabolism
Lipid metabolism
mTOR pathway
Glucocorticoid receptor pathway
Insulin like growth factor (IGF1) AKT signaling
AMPK signaling
Unfolded protein response (UPR)
Autophagy
NAD metabolism Sirtuins and Aging
GSK3 pathway
Canonical Pathways
Muscle structure development
DNA repair
Carbohydrate transport
Muscle cell differentiation
Regulation of muscle tissue regeneration
Glucose metabolism
Amino acid transport
Circadian rhythm
Mitochondrial membrane organization
GO BP
IL2 STAT5 signaling
Inflammatory reponse
PI3K AKT mTOR signaling
Angiogenesis
Hallmark
−Log10(P−value)
count
−log10(pvalue)